

LeAD-M3D: Leveraging Asymmetric Distillation for Real-time Monocular 3D Detection

Johannes Meier^{1,2,3,4,†,*}Jonathan Michel^{3,‡}Oussema Dhaouadi^{1,3,4}Yung-Hsu Yang²Christoph Reich^{3,4,5}Zuria Bauer²Stefan Roth⁵Marc Pollefeys^{2,6}Jacques Kaiser¹Daniel Cremers^{3,4}¹ DeepScenario² ETH Zurich³ TU Munich⁴ MCML⁵ TU Darmstadt⁶ Microsoft<https://deepscenario.github.io/LeAD-M3D/>

Abstract

Real-time monocular 3D object detection remains challenging due to severe depth ambiguity, viewpoint shifts, and the high computational cost of 3D reasoning. Existing approaches either rely on LiDAR or geometric priors to compensate for missing depth, or sacrifice efficiency to achieve competitive accuracy. We introduce *LeAD-M3D*, a monocular 3D detector that achieves state-of-the-art accuracy and real-time inference without extra modalities. Our method is powered by three key components. Asymmetric Augmentation Denoising Distillation (A2D2) transfers geometric knowledge from a clean-image teacher to a mixup-noised student via a quality- and importance-weighted depth-feature loss, enabling stronger depth reasoning without LiDAR supervision. 3D-aware Consistent Matching (CM_{3D}) improves prediction-to-ground truth assignment by integrating 3D MGIOU into the matching score, yielding more stable and precise supervision. Finally, Confidence-Gated 3D Inference (CGI_{3D}) accelerates detection by restricting expensive 3D regression to top-confidence regions. Together, these components set a new Pareto frontier for monocular 3D detection: *LeAD-M3D* achieves state-of-the-art accuracy on KITTI and Waymo, and the best reported car AP on Rope3D, while running up to $3.6\times$ faster than prior high-accuracy methods. Our results demonstrate that high fidelity and real-time efficiency in monocular 3D detection are simultaneously attainable—without LiDAR, stereo, or geometric assumptions.

1. Introduction

Monocular 3D Object Detection (M3D) aims to predict the 3D position, orientation, and size of objects from a sin-

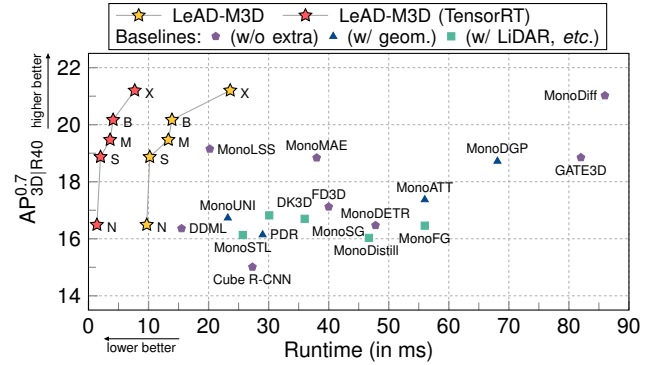


Figure 1. **Runtime vs. Accuracy** on the KITTI test set, using $AP_{3D|R40}^{0.7}$ Mod (in %, \uparrow) and runtime (in ms, \downarrow). We provide different model variants (N to X) to balance runtime and accuracy. *LeAD-M3D* offers a Pareto frontier over existing approaches. Our most accurate model outperforms the recent most accurate approach MonoDiff [69], while being $3.6\times$ faster. Using TensorRT further improves runtime, enabling real-time inference of even our largest model variant (X). For a fair comparison, all reported methods are re-evaluated on the same hardware (NVIDIA RTX 8000) if the code is publicly available.

gle RGB image. This setup is widely available and easy to deploy for autonomous driving [7, 14], robotics [42], medicine [1], and city infrastructure [72]. However, estimating depth information from a single 2D image plane introduces strong ambiguity, and is the dominant source of error in M3D [58, 92]. This problem only intensifies for viewpoint changes different from the training distribution [60, 99]. Moreover, recent methods emphasize accuracy over runtime efficiency [51, 69], which makes it hard to deploy for real-world scenarios. A model that learns exclusively from 3D box supervision, generalizes across viewpoints, and offers efficient inference remains lacking.

To resolve this ambiguity of the accuracy-efficiency trade-off, knowledge distillation (KD) for efficient student

*j.meier@tum.de [†] Equal contribution

models is a popular and powerful solution. In M3D, the main challenge is estimating depth information from the single 2D image plane [58]. Because of this, many methods use LiDAR [16, 28, 87, 88, 93] to create a teacher-student asymmetry, allowing the student to learn high-quality 3D geometric cues. However, in real-world applications, LiDAR-based supervision is not always available [17, 109]. Thus, we propose a LiDAR-free KD pipeline, which leverages the asymmetric denoising distillation [27] strategy to transfer knowledge from a strong teacher model to a lightweight student.

Unlike prior distillation approaches that give the teacher privileged data such as LiDAR depth [16, 18, 22, 87, 93], we propose *Asymmetric Augmentation Denoising Distillation* (A2D2). We build five M3D model variants with different model scales, *i.e.* N / S / M / B / X, following the YOLO family [83]. We train our largest variant (X) as a teacher model to provide expertise. Then, we freeze the teacher model and train the student model to denoise the mixup-augmented [100] input images, with the training supervised by matching the teacher’s object-level depth features computed from the clean input images. A dynamic feature loss further weights each channel according to the teacher’s prediction quality and the feature’s importance, focusing learning on reliable and informative cues. This process strengthens the student’s geometric reasoning without requiring any depth maps or extra modalities, such as LiDAR.

To complement A2D2, we introduce two additional components. *First*, we introduce 3D-aware Consistent Matching (CM_{3D}), which improves the prediction-to-ground truth assignment by incorporating a 3D Intersection over Union (IoU) term into the matching criterion. This joint 2D–3D alignment allows the model to learn from supervision that better reflects actual 3D localization quality. *Second*, we propose Confidence-Gated 3D Inference (CGI_{3D}), a lightweight inference strategy that restricts the costly 3D regression head to high-confidence regions identified by a fast 2D classifier. This reduces redundant computation and accelerates inference with no loss in accuracy. Together, we present **LeAD-M3D**, **L**everaging **A**symmetric **D**istillation for **R**ead-time **M**onocular **3D** **D**etection. These components yield a strong balance between accuracy and speed (*cf.* Fig. 1).

LeAD-M3D achieves state-of-the-art (SOTA) results across multiple benchmarks while running in real-time. On KITTI [23], we achieve the highest AP_{3D} across all difficulty levels among monocular methods and surpass even LiDAR- and geometry-assisted approaches, while running 3.6× faster than the next-best high-accuracy model. On Waymo [79], we improve over the previous best by 2.97 AP_{3D}^{0.5} (Level 1), and on Rope3D [99], we increase AP_{3D}^{0.7} for cars by 3.59 compared to the prior state of the art. Moreover, our second-largest model variant (B) still provides

the fastest runtime compared to all existing M3D methods. These results demonstrate that LeAD-M3D achieves high accuracy and real-time efficiency, all without relying on LiDAR, stereo, or ground-plane assumptions. We further showcase that LeAD-M3D exhibits strong cross-view generalization on Rope3D [99].

Our main contributions can be summarized as follows:

- We propose Asymmetric Augmentation Denoising Distillation (A2D2), a novel, LiDAR-free knowledge distillation scheme for M3D. It transfers geometric knowledge using mixup-based information asymmetry and a quality- and importance-weighted feature loss, strengthening the student’s depth reasoning without requiring privileged depth information.
- We introduce CM_{3D}, a dynamic task alignment strategy that significantly improves prediction-to-ground truth assignment by incorporating a 3D MGIOU term. This enables better object localization by aligning predictions based on both 2D and 3D geometric quality.
- We propose CGI_{3D}, a lightweight inference strategy that restricts the costly 3D regression head to high-confidence regions. This effectively reduces head-level FLOPs and enables real-time inference without any degradation in detection accuracy.
- We demonstrate the effectiveness of our LeAD-M3D on three established datasets, KITTI, Waymo, and Rope3D. LeAD-M3D obtains state-of-the-art accuracy on all datasets, without relying on LiDAR, stereo, or geometric priors, and provides a new Pareto frontier for the accuracy-efficiency trade-off (*cf.* Fig. 1).

2. Related Work

2.1. Monocular 3D object detection

Existing M3D methods can be broadly grouped into three categories. The first uses extra data, such as LiDAR [28, 66, 70, 87, 91, 97], object shape cues [43, 54], temporal consistency [13], ground planes [10, 76], or stereo images [19], during training to compensate for sparse 3D box supervision. The dependency on additional data limits applicability to real-world applications where these modalities are unavailable, *e.g.*, LiDAR is not present in certain traffic [81, 109] or drone [17, 60] views. The second family injects geometric constraints to regularize depth. A common assumption is that the apparent 2D height of an object is inversely proportional to its depth, which yields a scale prior by relating the estimated 3D height to the 2D height. Those methods [33, 68, 92, 108] encode variants of these priors. However, these constraints largely hold under car-view settings with near-zero roll and pitch but will restrict deployment to forward-facing automotive cameras [60, 99, 109]. The third family relies only on 3D bounding boxes for supervision without auxiliary modalities or hard-coded pri-

ors [20, 29, 31, 35, 47]. We focus on this category of models to maximize applicability across camera viewpoints and datasets. Our approach naturally fits this family because it allows for full flexibility with respect to object orientation, explicitly supporting arbitrary $SO(3)$ rotations rather than being constrained by viewpoint-specific priors like the inverse 2D height-depth relationship.

2.2. Knowledge distillation

knowledge distillation (KD) [5, 24, 59, 74] is a general technique for transferring knowledge from a highly accurate teacher model to improve a smaller student model’s accuracy without impacting its runtime. Previous M3D methods achieve this teacher–student asymmetry by giving the teacher an easier problem or more informative data, *e.g.*, giving LiDAR, allowing the monocular student to learn high-quality 3D geometric cues. On the other hand, ADD [87] and FD3D [88] remove the LiDAR dependency by providing the teacher with ground truth object positions or object-wise depth maps. Our approach takes a different angle on this paradigm. Instead of giving the teacher more information, we give the student strongly augmented mixup images [100], while the teacher receives both clean images. Moreover, compared to previous methods [16, 28, 87, 88, 93], we design the distillation loss dynamically weighted by the teacher’s prediction quality and feature importance, resulting in better distillation.

2.3. Real-time object detection

Real-time 2D detection [8, 38, 41, 56, 67, 82, 85, 104] has seen sustained progress on the accuracy–efficiency frontier. Among them, the YOLO series remains a prominent line of research [38, 41, 82], and we build our real-time M3D model based on YOLOv10 [83], which enables non-maximum suppression (NMS)-free inference at test time. Existing M3D methods require long [66, 70, 91] or moderate inference time [47, 52], and most provide only a single model size [47, 55, 92]. On the contrary, we follow YOLOv10 and have five model variants for different accuracy and efficiency tradeoffs. By introducing our A2D2, each variant raises its accuracy without extra inference cost. Moreover, our proposed CGI_{3D} for inference-side optimizations further reduces runtime by up to 30% with zero accuracy impact. This leads our second-largest model variant (B) to outperform the previous fastest baseline in speed.

3. Method

3.1. Problem statement

The goal of an M3D method is to estimate 3D bounding boxes and object categories from a single RGB image. Formally, let Im be an RGB image with an intrinsic camera matrix $K \in \mathbb{R}^{3 \times 3}$, and let $\hat{B}(\text{Im}) = \{\hat{b}_1^{3D}, \dots, \hat{b}_n^{3D}\}$ denote

the estimated 3D bounding boxes for objects in Im . Each box \hat{b}_i^{3D} is defined by its location $(x_i, y_i, z_i) \in \mathbb{R}^3$, dimensions $(w_i, h_i, l_i) \in \mathbb{R}^3$, orientation represented by a rotation matrix $R_i \in SO(3)$, and category $c_i \in C$ (*e.g.*, “vehicle”). For autonomous driving, R_i is often reduced to a single angle $\theta \in [-\pi, \pi]$, representing the yaw of the object.

3.2. Overview

Prior M3D methods largely optimize accuracy, while runtime efficiency is often secondary. We address this by introducing **Leveraging Asymmetric Distillation for Real-time Monocular 3D Detection (LeAD-M3D)**, a novel M3D method built on YOLOv10 [83]. As shown in Fig. 2 (b), we follow [47] and extend YOLOv10 with standard 3D detection heads, *i.e.* 3D offset, 3D dimension, orientation, depth and depth uncertainty heads, a postprocessing pipeline, and 3D losses. This baseline establishes an efficient architectural foundation for M3D, which we denote as YOLOv10-M3D. We show more details in the supplementary material. As shown in Fig. 2 (a), our overall pipeline further extends the baseline M3D model with three proposed components. **A2D2** enhances standard KD techniques by integrating a novel augmentation-based denoising task. **CM_{3D}** lifts the standard 2D prediction-to-ground truth assignment to 3D space. Finally, **CGI_{3D}** reduces head FLOPs during inference without impacting the predictions.

3.3. Asymmetric Augmentation Denoising Distillation (A2D2)

KD is an effective route to balance accuracy with real-time requirements. KD methods for M3D often create an information asymmetry by easing the teacher’s task. Since depth estimation is the core bottleneck in M3D, these methods [16, 28, 93] simplify the teacher’s predictions enormously by adding LiDAR depth [16, 28, 87, 88, 93]. This further strengthens the transfer for M3D yet introduces a modality dependency. Moreover, standard KD losses transfer all features uniformly [16, 28, 87, 88, 93]. Ignoring variation in the teacher’s quality and the varying influence of feature channels on the final depth. To address these issues, we propose **Asymmetric Augmentation Denoising Distillation (A2D2)**, a LiDAR-free KD scheme that couples an asymmetric mixup-based denoising task with quality- and importance-weighted feature alignment.

Mixup-based information asymmetry. Unlike previous methods, we leverage Mixup3D [47, 60] to augment the student input, enabling the student to learn to match the teacher’s instance-depth features despite augmentation, thereby creating the desired asymmetry without requiring extra modalities. In particular, we blend two images at the pixel level and require the student model to predict all objects for both images. Crucially, mixup preserves object geometry in image coordinates, *i.e.* projected centers, depths,

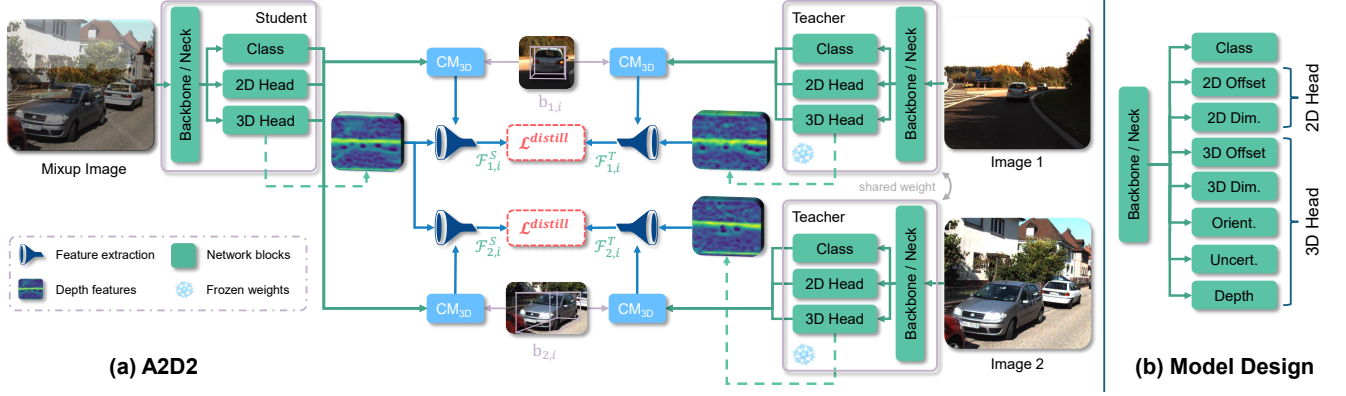


Figure 2. **Overview of LeAD-M3D.** (a) We distill high-dimensional instance-depth features from a large teacher to a compact student. To create an information gap, the teacher sees clean images. The student receives a mixup image and must reproduce the teacher’s intermediate features (Sec. 3.3). This frames distillation as a denoising task, which removes mixup-induced artifacts. $\text{CM}_{3\text{D}}$ uses ground truth to pair corresponding teacher and student predictions (*cf.* Sec. 3.4). (b) The model architecture in detail. *Dim.* stands for dimension head, *Orient.* stands for orientation head, and *Uncert.* stands for depth uncertainty head.

dimensions, and orientation remain consistent. We exploit this invariance to cast distillation as a denoising objective in feature space.

As shown in Fig. 2 (a), first, we feed two clean images to the teacher and the corresponding mixup image to the student. Second, we use 3D-aware Consistent Matching ($\text{CM}_{3\text{D}}$) (Sec. 3.4) to assign each ground truth object to its best matching prediction from the teacher and separately to its best match from the student. This establishes explicit student–teacher pairs for the same underlying object, enabling feature-level distillation between corresponding predictions. It is worth noting that we distill the depth features from the depth head rather than generic backbone activations, where the scalar depth is obtained by multiplying the depth features $\mathcal{F}_{n,i}^T \in \mathbb{R}^{64}$ by a weight matrix $W^T \in \mathbb{R}^{64}$. We found that depth features yield more effective transfer for the 3D task.

Quality- and importance-weighted distillation loss. To address that the standard KD losses ignore variation in teacher quality and the unequal influence of feature channels, we propose to reweight the feature loss with indicators measuring the prediction quality of the teacher and the importance of each feature. For the teacher’s quality, we weight the distillation loss by a score based on the relative depth error:

$$\eta_{n,i} = \frac{z_{n,i}}{\max(|z_{n,i} - \hat{z}_{n,i}^T|, \epsilon)}, \quad (1)$$

where $z_{n,i}$ and $\hat{z}_{n,i}^T$ denote ground truth and teacher-predicted depth for instance i in image n . We set $\epsilon = 0.1$ for stability. Using a relative error mitigates bias toward nearby objects, which naturally exhibit smaller absolute errors. For feature importance, the channels with larger abso-

lute weights contribute more to the final prediction. Therefore, we define the normalized importance per channel q as:

$$\omega_q = \frac{|W_q^T|}{\sum_{q'} |W_{q'}^T|}. \quad (2)$$

We now combine these weights with an L1 alignment over instance-depth features. Let I_n be the set of ground truth instances in image n matched to student–teacher predictions by $\text{CM}_{3\text{D}}$. Let $\mathcal{F}_{n,i,q}^T$ and $\mathcal{F}_{n,i,q}^S$ denote teacher and student instance-depth features for channel $q \in \{1, \dots, 64\}$. We define the quality- and importance-weighted feature-loss as:

$$\mathcal{L}^{\text{distill}} = \frac{1}{\sum_n |I_n|} \sum_n \sum_{i \in I_n} \sum_{q=1}^{64} \omega_q \eta_{n,i} |\mathcal{F}_{n,i,q}^T - \mathcal{F}_{n,i,q}^S|. \quad (3)$$

Training. We adopt offline KD with a frozen teacher. We first train the largest model variant X with standard supervision, *i.e.* classification loss \mathcal{L}^{cls} , 2D bounding box loss $\mathcal{L}^{2\text{D}}$, and 3D bounding box loss $\mathcal{L}^{3\text{D}}$, then freeze it as the teacher for student training. Then during A2D2 training, we supervise the student models with the total loss as:

$$\mathcal{L} = \mathcal{L}^{\text{cls}} + \mathcal{L}^{2\text{D}} + \mathcal{L}^{3\text{D}} + \mathcal{L}^{\text{distill}}, \quad (4)$$

while mixup is applied with probability 0.5. We show more details for training losses in the supplementary.

3.4. 3D-aware Consistent Matching ($\text{CM}_{3\text{D}}$)

Both supervised training and our A2D2 method require reliable assignments between model predictions and ground truth objects. Without robust matching, noisy or misaligned pairs can degrade both training stability and final accuracy,

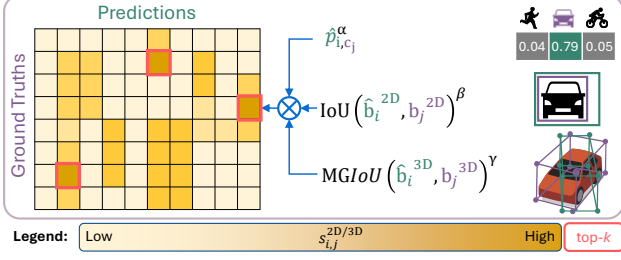


Figure 3. **3D-aware Consistent Matching (CM_{3D})**. Disambiguating prediction-to-ground truth assignments in crowded 3D scenes by integrating 2D and 3D overlaps (*cf.* Sec. 3.4).

especially in challenging scenarios like mixup, where multiple objects with similar 2D projections coexist. To address this, we propose **3D-aware Consistent Matching (CM_{3D})**, which ranks prediction-ground truth pairs using class confidence and both 2D and 3D box agreement.

The 2D matches in our baseline YOLOv10-M3D are determined by ranking all prediction-ground truth pairs using the score $s_{i,j}^{2D}$, and selecting the top- k pairs:

$$s_{i,j}^{2D} = \hat{p}_{i,c_j}^\alpha \cdot \text{IoU}(\hat{b}_i^{2D}, b_j^{2D})^\beta, \quad (5)$$

where i indexes predictions, j indexes ground truth, \hat{p}_{i,c_j} is the predicted probability for class c_j , \hat{b}_i^{2D} and b_j^{2D} are the predicted and ground truth 2D bounding boxes, and α, β are hyperparameters. We extend this to 3D by incorporating the Marginalized Generalized IoU (MGIoU) [40] between predicted and ground truth 3D boxes (*cf.* Fig. 3):

$$s_{i,j}^{2D/3D} = s_{i,j}^{2D} \cdot \text{MGIoU}(\hat{b}_i^{3D}, b_j^{3D})^\gamma, \quad (6)$$

with predicted and ground truth 3D bounding boxes \hat{b}_i^{3D} and b_j^{3D} and hyperparameter γ . MGIoU offers a 3D overlap surrogate that remains informative even without box intersection, which is common early in training or for small, distant objects. It aggregates location, size, and orientation, and is invariant to object dimensions, unlike corner-based losses [45].

Compared to static anchor-based assignments used in many M3D methods [52, 60], our dynamic 2D/3D scoring better disambiguates crowded scenes and mixed content (*e.g.*, under mixup). The 2D term stabilizes learning when 3D estimates are crude, while the 3D term helps to separate overlapping predictions as accuracy improves.

3.5. Confidence-Gated 3D Inference (CGI_{3D})

Many M3D detectors run their regression heads densely over full feature maps. As most locations correspond to background, a substantial portion of the computation is wasted. Therefore, we propose **Confidence-Gated 3D Inference (CGI_{3D})** to restrict expensive regression to likely object locations as shown in Fig. 4:

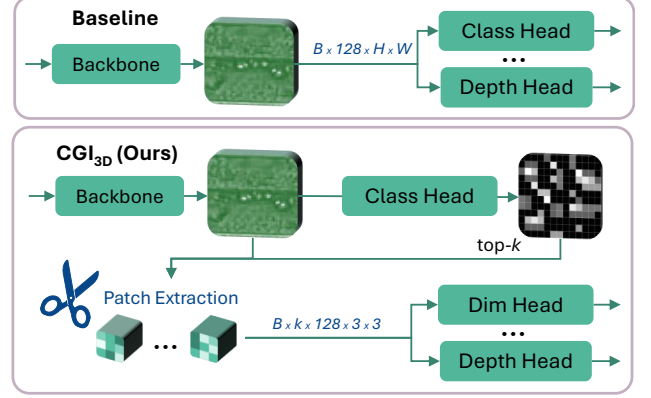


Figure 4. **Confidence-Gated 3D Inference (CGI_{3D})**: FLOP reduction and speedup by restricting 2D/3D regression to high-confidence locations (*cf.* Sec. 3.5).

1. After obtaining the neck features, we run inference on the classification head densely across the entire feature map.
2. We select the top- k locations by class confidence.
3. We extract 3×3 local patches centered at these locations.
4. Instead of applying them densely, we now apply the 2D and 3D regression heads only on these patches.

During training, we keep the dense head computation for simplicity. At inference, we move the baseline top- k selection earlier and run the 2D/3D heads only on 3×3 patches around top- k locations, yielding outputs identical to dense evaluation, because the heads’ effective receptive field is exactly 3×3 (one 3×3 conv followed by two 1×1 convs). This is simpler than Region of Interest (RoI) pooling (typically 7×7 grids [71]) and avoids bilinear interpolation, substantially reducing head-level FLOPs with no accuracy loss.

4. Experiments

4.1. Datasets and metrics

We evaluate our approach on the standard benchmarks for M3D: KITTI [23] and Waymo [79]. To demonstrate generalization across diverse camera perspectives, we include the traffic-view benchmark Rope3D [99] for comparison.

KITTI [23]. We use the standard split [9] (3,712 train, 3,769 val, 7,518 test). We report $\text{AP}_{3D|R40}(\text{primary})$ and $\text{AP}_{\text{BEV}|R40}(\text{secondary})$ on Easy/Mod./Hard difficulty levels, focusing on Mod. as the primary benchmark. We apply IoU thresholds of 0.7 for cars and 0.5 for pedestrians and cyclists.

Waymo [79]. Waymo is a large-scale car-view dataset. We use front-camera images (52,386 train, 39,848 val) following the protocol established by DEVIANT [39]. We report AP_{3D} and APH_{3D} at IoU thresholds of 0.5 and 0.7 for level 1 (L1) and level 2 (L2).

Rope3D [99]. We use the heterologous split (40,333 train,

Table 1. **Comparison with lightweight M3D methods (< 30M parameters) on the KITTI [23] test set for the car category.** *Extra* highlights methods that utilize auxiliary data during training to improve accuracy. *Params*: Million model parameters. *GFLOPs*: Giga FLOPs per image during inference time. *Time*: For a fair comparison, inference time is shown in ms for batch size 1 without TensorRT (hardware: NVIDIA RTX 8000).

Method	Extra	Params ↓	GFLOPs ↓	Time ↓	AP ^{0.7} _{3D R40} ↑			AP ^{0.7} _{BEV R40} ↑		
					Easy	Mod.	Hard	Easy	Mod.	Hard
MonoNERD [91]	LiDAR	6.6	4 220	1 380.3	22.75	17.13	15.63	31.13	23.46	20.97
MonoSGC [32]	LiDAR	23.1	173	35.0	27.01	16.77	14.61	35.78	23.27	19.92
OccupancyM3D [66]	LiDAR	28.3	389	213.9	25.55	17.02	14.79	35.38	24.18	21.37
DPL _{FLEX} [101]	Unlabeled	21.5	152	28.9	24.19	16.67	13.83	33.16	22.12	18.74
MonoUNI [33]	Geometry	22.7	122	23.2	24.75	16.73	13.49	33.28	23.05	16.39
MonoCD [92]	Geometry	21.8	171	28.1	25.53	16.59	14.53	33.41	22.81	19.57
MonoCon [52]	—	19.6	115	15.5	22.50	16.46	13.95	31.12	22.10	19.00
DDML [15]	—	19.6	115	15.5	23.31	16.36	13.73	—	—	—
MonoLSS [47]	—	21.5	127	20.2	26.11	19.15	16.94	34.89	25.95	22.59
LeAD-M3D N (Ours)	—	3.8	14	9.7	24.31	16.49	14.14	32.22	21.72	19.41
LeAD-M3D S (Ours)	—	10.1	38	10.2	27.28	18.87	16.37	34.86	24.17	21.32
LeAD-M3D M (Ours)	—	19.7	88	13.3	28.08	19.47	17.66	36.21	25.46	22.89
LeAD-M3D B (Ours)	—	24.9	133	13.9	29.10	20.17	18.34	37.65	26.63	23.75

4,676 val), a more challenging setting with changing camera views. Accuracy is evaluated using AP_{3D|R40} and the Rope [99] score at IoU thresholds of 0.5 and 0.7 for Mod. difficulty, considering the car and big vehicle classes.

4.2. Comparison with lightweight M3D models

In Tab. 1, we compare our model with lightweight M3D methods in terms of accuracy, FLOPs, model size, and run-time. MonoNeRD [91] uses fewer parameters than any prior method (6.6M). Despite this, our second-smallest model (S) surpasses MonoNeRD in accuracy while being trained LiDAR-free; notably, it runs over 100× faster at inference. We trace the surprisingly low speed of MonoNeRD to its compute-heavy 3D volume processing, which dominates its latency. In terms of FLOPs, our third-largest model (M) requires 25 % fewer FLOPs than the fastest alternatives, DDML [15] and MonoCon [52], yet outperforms all existing methods on 5 out of 6 metrics. Our second-largest model (B size) maintains a faster runtime than the fastest existing lightweight baseline while surpassing all prior methods in accuracy.

4.3. Comparison with SOTA M3D models

KITTI [23] test set. In Tab. 2, we compare our largest model LeAD-M3D X with SOTA models on the KITTI test set (requiring submission to the test server). LeAD-M3D outperforms all existing methods in AP_{3D|R40}, including those that leverage geometric priors or extra training data. Furthermore, our model runs 3.6× faster than the previous SOTA MonoDiff [69] (*cf.* supplementary material).

Waymo [79] validation set. Similarly, our largest model (X) achieves the best results on the Waymo validation

Table 2. **Comparison with state-of-the-art (SOTA) monocular methods on the KITTI [23] test set for the car category.** *Extra* highlights methods that utilize auxiliary data during training to improve accuracy.

Method	Extra	AP ^{0.7} _{3D R40} ↑		
		Easy	Mod.	Hard
MonoDistill [16]	LiDAR	24.31	18.47	15.76
ADD [87]	LiDAR	25.61	16.81	13.79
HSRDN [93]	LiDAR	22.01	13.61	13.10
MonoFG [22]	LiDAR	24.35	16.46	13.84
MonoSTL [18]	LiDAR	25.33	16.13	13.35
MonoSG [19]	Stereo	25.77	16.70	14.22
DK3D [89]	LiDAR	25.63	16.82	13.81
MonoTAKD [51]	LiDAR	27.91	19.43	16.51
DA3D [34]	Geometry	27.76	20.47	17.89
MoGDE [108]	Geometry	27.25	17.93	15.80
MonoDGP [68]	Geometry	26.35	18.72	15.97
Cube R-CNN [4]	—	23.59	15.01	12.56
MonoDETR [102]	—	25.00	16.47	16.38
MonoPSTR [95]	—	26.15	17.01	13.70
FD3D [88]	—	25.38	17.12	14.50
MonoDiff [69]	—	30.18	21.02	18.16
MonoMAE [35]	—	25.60	18.84	16.78
GATE3D [31]	—	26.07	18.85	16.76
LeAD-M3D X (Ours)	—	30.76	21.20	18.76

set [79] (see Tab. 3) without geometric assumptions or extra training data. For AP^{0.5}_{3D} Level 1, we surpass the previous best model [47] by 2.97 AP. Even our second-largest model (B) attains a higher AP^{0.5}_{3D} than all existing methods.

Rope3D [99] validation set. In Tab. 4, we compare our approach on Rope3D [99] (traffic view). LeAD-M3D scores the best result for the car category. For the rare category big vehicle, it performs second-best to

Table 3. **Comparison with SOTA monocular methods on the Waymo [79] validation set for the vehicle category.** We compare with methods that use the same training and validation set as in DEVIANT [39].

Method	AP _{3D} ^{0.5} ↑		AP _{3D} ^{0.7} ↑	
	L1	L2	L1	L2
PatchNet [57]	2.92	2.42	0.39	0.38
PCT [84]	4.20	4.03	0.89	0.66
GUPNet [55]	10.02	9.39	2.28	2.14
DEVIANT [39]	10.98	10.29	2.69	2.52
MonoJSG [49]	5.65	5.34	0.97	0.91
MonoCon [52]	10.07	9.44	2.30	2.16
Stereoscopic [36]	7.18	7.17	1.72	1.61
MonoRCNN++ [77]	11.37	10.79	4.28	4.05
MonoUNI [33]	10.98	10.38	3.20	3.04
MonoXiver-GUPNet [53]	11.47	10.67	—	—
MonoXiver-DEVIANT [53]	11.88	11.06	—	—
DDML [15]	10.14	9.50	2.50	2.34
MonoAux [48]	9.82	9.25	3.92	3.57
NF-DVT [63]	11.32	11.24	2.76	2.64
MonoLSS [47]	13.49	13.12	3.71	3.27
SSD-MonoDETR [26]	11.83	11.34	4.54	4.12
GroundMix [60]	11.89	10.50	3.10	2.73
MonoCD [92]	11.62	11.14	3.85	3.50
MonoDGP [68]	12.36	11.71	4.28	4.00
LeAD-M3D N (Ours)	12.14	10.73	2.96	2.61
LeAD-M3D S (Ours)	13.24	12.08	3.53	3.11
LeAD-M3D M (Ours)	14.55	12.86	3.98	3.51
LeAD-M3D B (Ours)	15.04	13.29	4.29	3.78
LeAD-M3D X (Ours)	16.46	14.54	4.82	4.24

Table 4. **Comparison with SOTA monocular methods on the Rope3D heterologous benchmark [99].** *GPF* highlights methods that do not require ground plane [76, 96, 99] input. We report AP_{3D|R40}^{0.7} and Rope score [99] for cars and big vehicles (BV).

Method	GPF	Car ↑		BV ↑	
		AP	Rope	AP	Rope
M3D-RPN [2]	✗	11.09	28.17	3.39	21.01
MonoDLE [58]	✗	12.16	28.39	3.02	19.96
MonoFlex [103]	✗	11.24	27.79	13.10	28.22
BEVHeight [96]	✗	5.41	23.09	1.16	18.53
CoBEV [76]	✗	6.59	24.01	2.26	19.71
M3D-RPN [2]	✓	6.05	23.84	2.78	20.82
Kinematic3D [3]	✓	5.82	23.06	1.27	18.92
MonoDLE [58]	✓	3.77	21.42	2.31	19.55
MonoFlex [103]	✓	10.86	27.39	0.97	18.18
BEVFormer [46]	✓	3.87	21.84	0.84	18.42
BEVDepth [44]	✓	0.85	19.38	0.30	17.84
MonoCon [52]	✓	10.71	27.55	1.61	19.25
GroundMix [60]	✓	12.86	29.37	3.90	21.06
LeAD-M3D N (Ours)	✓	9.67	25.46	1.80	19.17
LeAD-M3D S (Ours)	✓	13.33	28.59	4.16	21.25
LeAD-M3D M (Ours)	✓	14.31	29.62	4.95	22.14
LeAD-M3D B (Ours)	✓	15.05	30.13	5.40	22.41
LeAD-M3D X (Ours)	✓	16.45	31.34	8.71	25.15

Table 5. **Ablation study on the effectiveness of the CM_{3D}** (*cf.* Sec. 3.4) and the A2D2 (*cf.* Sec. 3.3). Experiments are conducted on the KITTI [23] validation set. The first line and last line denote the baseline YOLOv10-M3D B and LeAD-M3D B, respectively.

A2D2	CM _{3D}		Car AP _{3D R40} ^{0.7}		
	2D IoU	3D MGIOU	Easy ↑	Mod. ↑	Hard ↑
1	✓		25.68	19.60	17.47
2	✓	✓	26.26	20.43	17.71
3	✓	✓	27.12	21.81	19.34
4	✓	✓	26.34	21.49	19.12
5	✓	✓	28.33	22.72	19.98

MonoFlex [103] with ground plane input. In a fair comparison (*i.e.*, the ground plane is not given to MonoFlex), our AP_{3D|R40} on big vehicle is substantially higher than MonoFlex.

4.4. Ablation study

We conduct our ablation study on the KITTI [23] validation set and report AP_{3D|R40}^{0.7} on the Mod. split. All ablations use the B model.

Main ablation. Tab. 5 analyzes the contributions of the proposed CM_{3D} and Distill components. The full model (row 5) achieves a substantial 2.67 AP gain over the baseline (row 1). Integrating CM_{3D} (row 2) contributes 0.83 AP, and the 1.23 AP drop when excluding the 2D IoU term (row 4) underscores the critical need for combining 2D and 3D cues. Crucially, the Distill module (row 3) which is our primary contribution yields the largest single boost of +2.29 AP, affirming its role as the key driver of the overall result.

A2D2 ablation. In Tab. 6, we conduct an ablation study on the key components of our A2D2 framework. Distilling backbone features reduces AP by 0.42, confirming that depth features are a more effective KD target than generic backbone features. Removing the feature-importance indicator reduces AP by 0.68, slightly more than removing the teacher-quality indicator (0.44 AP), indicating channel selectivity is the stronger weighting mechanism. Performing online instead of offline distillation reduces AP by 0.92, likely because the strongest distillation targets emerge only late in training, coinciding with the learning rate decay necessary for depth convergence. Finally, feeding the teacher the same mixup image as the student, *i.e.* removing the clean-mixed asymmetry, yields the largest decline of 1.15 AP, confirming that denoising is essential to A2D2’s effectiveness.

Runtime ablation. We evaluate the runtime of LeAD-M3D N in Tab. 7, detailing the impact of our two main modifications over the baseline: reducing the head channel dimensions from 128 to 64, and applying CGI_{3D}. The channel reduction yields a minor runtime decrease (0.7ms) and reduces FLOPs by ca. 40%, while AP remains roughly the

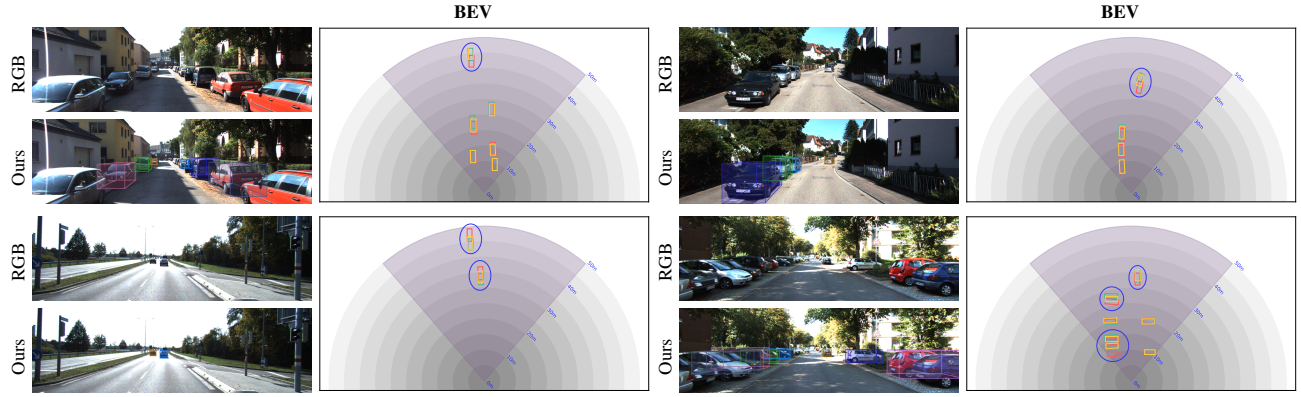


Figure 5. **Qualitative results on the KITTI [23] validation set.** LeAD-M3D X achieves more accurate depth estimates than YOLOv10-M3D X. Best viewed in color and with zoom. **Bird’s-eye view (BEV) color coding:** Ground truth, YOLOv10-M3D X, LeAD-M3D X, and field of view.

Table 6. **Detailed ablation study on A2D2** (cf. Sec. 3.3). We report $AP_{3D|R40}^{0.7}$ for cars on the KITTI [23] validation set using the B model. Results are sorted according to model accuracy.

Method	Easy \uparrow	Mod. \uparrow	Hard \uparrow
LeAD-M3D B (Ours)	28.33	22.72	19.98
Ours w/ backbone features	27.56	22.30	19.82
Ours w/o quality indicator	27.79	22.28	19.63
Ours w/o importance indicator	27.33	22.04	19.37
Ours w/ online self-distillation	27.45	21.80	19.57
Ours w/o clean images	17.19	21.57	19.27
Ours w/o A2D2	26.26	20.43	17.71

same. In contrast, applying CGI_{3D} alone reduces runtime by two-thirds and total FLOPs by ca. 75%. By combining both optimizations, we achieve a total runtime reduction of 40% and an overall FLOPs decrease of over 80%. The exceptional efficacy of CGI_{3D} stems from the fact that 3D head computation forms a significant bottleneck; as the heads maintain a fixed channel dimension while the backbone scales (e.g., smaller YOLO models), their computational cost becomes disproportionately large. A closer analysis (cf. supplementary material) shows that CGI_{3D} directly targets this issue, achieving a 6.79ms reduction in 2D/3D head computation which heavily compensates for its minor 0.26ms overhead for patch extraction.

4.5. Qualitative results

In Fig. 5 we show qualitative results on the KITTI [23] validation set. Our method produces noticeably more accurate depth estimates, particularly for moderate- and far-range objects where monocular depth is most challenging. We attribute these improvements primarily to the denoising-enhanced distillation (A2D2), which helps the compact student recover geometric cues under strong augmentations. Additional qualitative results on Rope3D [99] are provided in the supplementary material.

Table 7. **Ablation study on the effectiveness of our speedups** (Sec. 3.5). We evaluate the design choices on the KITTI validation set using the N model. **Ch.:** Number of channels in the regression heads. **AP:** Car Moderate accuracy is reported on the KITTI [23] validation set. **Time:** KITTI runtime in ms.

CGI_{3D}	Ch.	$AP_{3D R40}^{0.7} \uparrow$	GFLOPs \downarrow	Time \downarrow
✓	128	18.33	81.0	16.2
	128	18.33	19.5	10.9
✓	64	18.41	45.8	15.5
	64	18.41	14.4	9.7

5. Conclusion

We presented LeAD-M3D, a monocular 3D detection framework that unifies asymmetric geometric distillation, 3D-aware matching, and confidence-gated inference to achieve state-of-the-art accuracy with real-time efficiency—without LiDAR, stereo, or geometric priors. By strengthening depth reasoning through denoising-based distillation and allocating computation adaptively, LeAD-M3D establishes a new Pareto frontier for monocular 3D perception across KITTI, Waymo, and Rope3D.

LeAD-M3D opens several promising research directions. First, extending asymmetric distillation to leverage large-scale unlabeled data—for example, through self-supervised or teacher-free denoising—could further enhance the scalability and robustness of monocular 3D models. Second, while our method generalizes well across multiple datasets, developing a domain-agnostic 3D detector capable of zero-shot transfer to unseen environments is an exciting problem. Finally, integrating our framework into temporal or multi-view settings is another open challenge.

Overall, LeAD-M3D demonstrates that accurate, real-time monocular 3D detection is not only feasible but a viable foundation for broader advances in scalable 3D vision.

Acknowledgments This work is a result of the joint research project STADT:up. The project is supported by the German Federal Ministry for Economic Affairs and Climate Action (BMWK), based on a decision of the German Bundestag. The author is solely responsible for the content of this publication. This work was also supported by the ERC Advanced Grant SIMULACRON, the Georg Nemetschek Institute project AI4TWINNING and the DFG project 4D-YouTube CR 250/26-1.

References

- [1] Tina Boroukhian, Kritkorn Supyen, Jhealyn Bautista Samson, Atit Bashyal, and Hendro Wicaksono. Integrating 3D object detection with ontologies for accurate digital twin creation in manufacturing systems. *Int. J. Adv. Manuf. Technol.*, 140(9):4679–4711, 2025. [1](#)
- [2] Garrick Brazil and Xiaoming Liu. M3D-RPN: Monocular 3D region proposal network for object detection. In *ICCV*, pages 9286–9295, 2019. [7](#), [ix](#), [x](#)
- [3] Garrick Brazil, Gerard Pons-Moll, Xiaoming Liu, and Bernt Schiele. Kinematic 3D object detection in monocular video. In *ECCV*, pages 135–152, 2020. [7](#), [ix](#)
- [4] Garrick Brazil, Abhinav Kumar, Julian Straub, Nikhila Ravi, Justin Johnson, and Georgia Gkioxari. Omni3D: A large benchmark and model for 3D object detection in the wild. In *CVPR*, pages 13154–13164, 2023. [6](#), [ii](#), [vii](#), [viii](#)
- [5] Guobin Chen, Wongun Choi, Xiang Yu, Tony X. Han, and Manmohan Chandraker. Learning efficient object detection models with knowledge distillation. In *NeurIPS*, pages 742–751, 2017. [3](#)
- [6] Hansheng Chen, Yuyao Huang, Wei Tian, Zhong Gao, and Lu Xiong. MonoRUN: Monocular 3D object detection by reconstruction and uncertainty propagation. In *CVPR*, pages 10379–10388, 2021. [viii](#)
- [7] Li Chen, Penghao Wu, Kashyap Chitta, Bernhard Jaeger, Andreas Geiger, and Hongyang Li. End-to-end autonomous driving: Challenges and frontiers. *IEEE Trans. Pattern Anal. Mach. Intell.*, 46(12):10164–10183, 2024. [1](#)
- [8] Qiang Chen, Xiangbo Su, Xinyu Zhang, Jian Wang, Jiahui Chen, Yunpeng Shen, Chuchu Han, Ziliang Chen, Weixiang Xu, Fanrong Li, Shan Zhang, Kun Yao, Errui Ding, Gang Zhang, and Jingdong Wang. LW-DETR: A transformer replacement to YOLO for real-time detection. *arXiv:2406.03459 [cs.CV]*, 2024. [3](#)
- [9] Xiaozhi Chen, Kaustav Kundu, Yukun Zhu, Andrew G Berneshawi, Huimin Ma, Sanja Fidler, and Raquel Urtasun. 3D object proposals for accurate object class detection. *NIPS*, 28, 2015. [5](#)
- [10] Xiahao Chen, Mingjian Chen, Sanli Tang, Yi Niu, and Jiang Zhu. MOSE: Boosting vision-based roadside 3D object detection with scene cues. *arXiv:2404.05280 [cs.CV]*, 2024. [2](#), [ix](#)
- [11] Yongjian Chen, Lei Tai, Kai Sun, and Mingyang Li. MonoPair: Monocular 3D object detection using pairwise spatial relationships. In *CVPR*, pages 12090–12099, 2020. [viii](#)
- [12] Yi-Nan Chen, Hang Dai, and Yong Ding. Pseudo-stereo for monocular 3D object detection in autonomous driving. In *CVPR*, pages 877–887, 2022. [viii](#)
- [13] Haoran Cheng, Liang Peng, Zheng Yang, Binbin Lin, Xiaofei He, and Boxi Wu. Temporal feature fusion for 3D detection in monocular video. *IEEE Trans. Image Process.*, 33:2665–2675, 2024. [2](#)
- [14] Pranav Singh Chib and Pravendra Singh. Recent advancements in end-to-end autonomous driving using deep learning: A survey. *IEEE Trans. Intell. Veh.*, 9(1):103–118, 2024. [1](#)
- [15] Wonhyeok Choi, Mingyu Shin, and Sunghoon Im. Depth-discriminative metric learning for monocular 3D object detection. In *NeurIPS*, pages 80165–80177, 2023. [6](#), [7](#), [vi](#), [vii](#), [viii](#)
- [16] Zhiyu Chong, Xinzhu Ma, Hong Zhang, Yuxin Yue, Haojie Li, Zhihui Wang, and Wanli Ouyang. MonoDistill: Learning spatial features for monocular 3D object detection. In *ICLR*, 2022. [2](#), [3](#), [6](#), [vi](#), [vii](#), [viii](#)
- [17] Oussema Dhaouadi, Johannes Meier, Luca Wahl, Jacques Kaiser, Luca Scalerandi, Nick Wandelburg, Zhuolun Zhou, Nijanthan Berinpanathan, Holger Banzhaf, and Daniel Cremers. Highly accurate and diverse traffic data: The deep-scenario open 3D dataset. In *IV*, pages 377–384, 2025. [2](#)
- [18] Rui Ding, Meng Yang, and Nanning Zheng. Selective transfer learning of cross-modality distillation for monocular 3D object detection. *IEEE Trans. Circuits Syst. Video Technol.*, 34(10):9925–9938, 2024. [2](#), [6](#), [vi](#), [vii](#)
- [19] Zhiwei Fan, Chao Xu, Minghang Chu, Yuling Huang, Yaoyao Ma, Jing Wang, Yishen Xu, and Di Wu. MonoSG: Monocular 3D object detection with stereo guidance. *IEEE Robotics Autom. Lett.*, 10(4):3604–3611, 2025. [2](#), [6](#), [vi](#), [vii](#), [viii](#)
- [20] Tobias Fischer, Yung-Hsu Yang, Suryansh Kumar, Min Sun, and Fisher Yu. CC-3DT: Panoramic 3D object tracking via cross-camera fusion. In *CoRL*, 2022. [3](#)
- [21] Youjia Fu, Zihao Xu, Junsong Fu, Huixia Xue, Shuqiu Tan, Lei Li, and Shaoxun Qing. MonoMM: A multi-scale mamba-enhanced network for real-time monocular 3D object detection. *J. Supercomput.*, 81(3):449, 2025. [viii](#)
- [22] Honghao Gao, Xinxin Yu, Yueshen Xu, Qionghuizi Ran, and Walayat Hussain. MonoFG: Monocular 3D object detection with knowledge distillation for human-centric autonomous driving systems. *ACM Trans. Auton. Adapt. Syst.*, 2024. [2](#), [6](#), [vi](#), [vii](#)
- [23] Andreas Geiger, Philip Lenz, and Raquel Urtasun. Are we ready for autonomous driving? the KITTI vision benchmark suite. In *CVPR*, pages 3354–3361, 2012. [2](#), [5](#), [6](#), [7](#), [8](#), [i](#), [ii](#), [iii](#), [iv](#), [v](#), [vi](#), [vii](#), [viii](#), [ix](#), [xi](#)
- [24] Jianping Gou, Baosheng Yu, Stephen J. Maybank, and Dacheng Tao. Knowledge distillation: A survey. *Int. J. Comput. Vis.*, 129(6):1789–1819, 2021. [3](#)
- [25] Jiaqi Gu, Bojian Wu, Lubin Fan, Jianqiang Huang, Shen Cao, Zhiyu Xiang, and Xian-Sheng Hua. Homography loss for monocular 3D object detection. In *CVPR*, pages 1070–1079, 2022. [vi](#), [viii](#)
- [26] Xuan He, Fan Yang, Kailun Yang, Jiacheng Lin, Hao-long Fu, Meng Wang, Jin Yuan, and Zhiyong Li. SSD-MonoDETR: Supervised scale-aware deformable transformer for monocular 3D object detection. *IEEE Trans. Intell. Veh.*, 9(1):555–567, 2024. [7](#), [viii](#)

- [27] Geoffrey E. Hinton, Oriol Vinyals, and Jeffrey Dean. Distilling the knowledge in a neural network. *arXiv:1503.02531 [stat.ML]*, 2015. 2
- [28] Yu Hong, Hang Dai, and Yong Ding. Cross-modality knowledge distillation network for monocular 3D object detection. In *ECCV*, pages 87–104, 2022. 2, 3, vii, viii, x
- [29] Hou-Ning Hu, Qi-Zhi Cai, Dequan Wang, Ji Lin, Min Sun, Philipp Krähenbühl, Trevor Darrell, and Fisher Yu. Joint monocular 3D vehicle detection and tracking. In *ICCV*, pages 5390–5399, 2019. 3
- [30] Kuan-Chih Huang, Tsung-Han Wu, Hung-Ting Su, and Winston H. Hsu. MonoDTR: Monocular 3D object detection with depth-aware transformer. In *CVPR*, pages 4002–4011, 2022. viii
- [31] Eunsoo Im, Jung Kwon Lee, and Changhyun Jee. GATE3D: Generalized attention-based task-synergized estimation in 3D. In *CVPRW*, 2025. 3, 6, vii, viii
- [32] Yinshuai Ji and Jinhua Xu. Depth estimation from surface-ground correspondence for monocular 3D object detection. *IEEE Trans. Intell. Transp. Syst.*, 25(11):16312–16322, 2024. 6, vi, vii
- [33] Jinrang Jia, Zhenjia Li, and Yifeng Shi. MonoUNI: A unified vehicle and infrastructure-side monocular 3D object detection network with sufficient depth clues. In *NeurIPS*, 2023. 2, 6, 7, vi, vii, viii
- [34] Yisong Jia, Jue Wang, Huihui Pan, and Weichao Sun. Enhancing monocular 3-D object detection through data augmentation strategies. *IEEE Trans. Instrum. Meas.*, 73:1–11, 2024. 6, vi, vii, viii
- [35] Xueying Jiang, Sheng Jin, Xiaoqin Zhang, Ling Shao, and Shijian Lu. MonoMAE: Enhancing monocular 3D detection through depth-aware masked autoencoders. In *NeurIPS*, 2024. 3, 6, vi, vii
- [36] Jung Uk Kim, Hyung-II Kim, and Yong Man Ro. Stereoscopic vision recalling memory for monocular 3D object detection. *IEEE Trans. Image Process.*, 32:2749–2760, 2023. 7
- [37] Diederik P. Kingma and Jimmy Ba. Adam: A method for stochastic optimization. In *ICLR*, 2015. ii
- [38] Manikanta Kotthapalli, Deepika Ravipati, and Reshma Bhatia. YOLOv1 to YOLOv11: A comprehensive survey of real-time object detection innovations and challenges. *CoRR*, 2025. 3
- [39] Abhinav Kumar, Garrick Brazil, Enrique Corona, Armin Parchami, and Xiaoming Liu. DEVIANT: Depth equivariant network for monocular 3D object detection. In *ECCV*, pages 664–683, 2022. 5, 7, vi, vii, viii, x
- [40] Duy-Tho Le, Trung Pham, Jianfei Cai, and Hamid Rezatofighi. Marginalized generalized IoU (MGIoU): A unified objective function for optimizing any convex parametric shapes. *arXiv:2504.16443 [cs.CV]*, 2025. 5, xi
- [41] Mengqi Lei, Siqi Li, Yihong Wu, Han Hu, You Zhou, Xinhu Zheng, Guiguang Ding, Shaoyi Du, Zongze Wu, and Yue Gao. YOLOv13: Real-time object detection with hypergraph-enhanced adaptive visual perception. *arXiv:2506.17733 [cs.CV]*, 2025. 3
- [42] Mingxing Li and Nan Ma. Overview of 3D object detection for robot environment perception. In *ICIVIS*, pages 675–681, 2023. 1
- [43] Yingyan Li, Yuntao Chen, Jiawei He, and Zhaoxiang Zhang. Densely constrained depth estimator for monocular 3D object detection. In *ECCV*, pages 718–734, 2022. 2, viii
- [44] Yin hao Li, Zheng Ge, Guanyi Yu, Jinrong Yang, Zengran Wang, Yukang Shi, Jianjian Sun, and Zeming Li. BEVDepth: Acquisition of reliable depth for multi-view 3D object detection. In *AAAI*, pages 1477–1485, 2023. 7, ix
- [45] Zhuoling Li, Zhan Qu, Yang Zhou, Jianzhuang Liu, Haoqian Wang, and Lihui Jiang. Diversity matters: Fully exploiting depth clues for reliable monocular 3D object detection. In *CVPR*, pages 2781–2790, 2022. 5, vi, viii
- [46] Zhiqi Li, Wenhao Wang, Hongyang Li, Enze Xie, Chonghao Sima, Tong Lu, Yu Qiao, and Jifeng Dai. BEVFormer: Learning bird’s-eye-view representation from multi-camera images via spatiotemporal transformers. In *ECCV*, pages 1–18, 2022. 7, ix
- [47] Zhenjia Li, Jinrang Jia, and Yifeng Shi. MonoLSS: Learnable sample selection for monocular 3D detection. In *3DV*, pages 1125–1135, 2024. 3, 6, 7, i, iii, iv, vi, vii, viii
- [48] Zhenglin Li, Wenbo Zheng, Le Yang, Liyan Ma, Yang Zhou, and Yan Peng. MonoAux: Fully exploiting auxiliary information and uncertainty for monocular 3D object detection. *Cyborg Bionic Syst.*, 5:0097, 2024. 7
- [49] Qing Lian, Peiliang Li, and Xiaozhi Chen. MonoJSG: Joint semantic and geometric cost volume for monocular 3D object detection. In *CVPR*, pages 1060–1069, 2022. 7, viii
- [50] Tsung-Yi Lin, Michael Maire, Serge J. Belongie, James Hays, Pietro Perona, Deva Ramanan, Piotr Dollár, and C. Lawrence Zitnick. Microsoft COCO: Common objects in context. In *ECCV*, pages 740–755, 2014. iv, v
- [51] Hou-I Liu, Christine Wu, Jen-Hao Cheng, Wenhao Chai, Shian-Yun Wang, Gaowen Liu, Jenq-Neng Hwang, Hong-Han Shuai, and Wen-Huang Cheng. MonoTAKD: Teaching assistant knowledge distillation for monocular 3D object detection. In *CVPR*, pages 22266–22275, 2025. 1, 6, v, vi, vii, viii
- [52] Xianpeng Liu, Nan Xue, and Tianfu Wu. Learning auxiliary monocular contexts helps monocular 3D object detection. In *AAAI*, pages 1810–1818, 2022. 3, 5, 6, 7, vi, vii, viii, ix
- [53] Xianpeng Liu, Ce Zheng, Kelvin Cheng, Nan Xue, Guojun Qi, and Tianfu Wu. Monocular 3D object detection with bounding box denoising in 3D by perceiver. In *ICCV*, pages 6413–6423, 2023. 7
- [54] Zongdai Liu, Dingfu Zhou, Feixiang Lu, Jin Fang, and Liangjun Zhang. AutoShape: Real-time shape-aware monocular 3D object detection. In *ICCV*, pages 15621–15630, 2021. 2, viii
- [55] Yan Lu, Xinzhu Ma, Lei Yang, Tianzhu Zhang, Yating Liu, Qi Chu, Junjie Yan, and Wanli Ouyang. Geometry uncertainty projection network for monocular 3D object detection. In *ICCV*, pages 3091–3101, 2021. 3, 7, viii
- [56] Wenyu Lv, Yian Zhao, Qinyao Chang, Kui Huang, Guanzhong Wang, and Yi Liu. RT-DETRv2: Improved

- baseline with bag-of-freebies for real-time detection transformer. *arXiv:2407.17140 [cs.CV]*, 2024. 3
- [57] Xinzhu Ma, Shinan Liu, Zhiyi Xia, Hongwen Zhang, Xingyu Zeng, and Wanli Ouyang. Rethinking pseudo-LiDAR representation. In *ECCV*, pages 311–327, 2020. 7
- [58] Xinzhu Ma, Yinmin Zhang, Dan Xu, Dongzhan Zhou, Shuai Yi, Haojie Li, and Wanli Ouyang. Delving into localization errors for monocular 3D object detection. In *CVPR*, pages 4721–4730, 2021. 1, 2, 7, ix
- [59] Amir M. Mansourian, Rozhan Ahmadi, Masoud Ghafouri, Amir Mohammad Babaei, Elaheh Badali Golezani, Zeynab Yasamani Ghamchi, Vida Ramezani, Alireza Taherian, Kimia Dinashi, Amirali Miri, and Shohreh Kasaei. A comprehensive survey on knowledge distillation. *Trans. Mach. Learn. Res.*, 2025. 3
- [60] Johannes Meier, Luca Scalerandi, Oussema Dhaouadi, Jacques Kaiser, Araslanov Nikita, and Daniel Cremers. CARLA Drone: Monocular 3D object detection from a different perspective. In *GCPR*, 2024. 1, 2, 3, 5, 7, ii, iii, ix
- [61] Johannes Meier, Louis Inchingolo, Oussema Dhaouadi, Yan Xia, Jacques Kaiser, and Daniel Cremers. MonoCT: Overcoming monocular 3D detection domain shift with consistent teacher models. In *ICRA*, pages 351–358. IEEE, 2025. ii
- [62] Arsalan Mousavian, Dragomir Anguelov, John Flynn, and Jana Kosecka. 3D bounding box estimation using deep learning and geometry. In *CVPR*, pages 5632–5640, 2017. ii
- [63] Cong Pan, Junran Peng, and Zhaoxiang Zhang. Depth-guided vision transformer with normalizing flows for monocular 3D object detection. *IEEE CAA J. Autom. Sinica*, 11(3):673–689, 2024. 7
- [64] Dennis Park, Rares Ambrus, Vitor Guizilini, Jie Li, and Adrien Gaidon. Is pseudo-LiDAR needed for monocular 3D object detection? In *ICCV*, pages 3122–3132, 2021. viii
- [65] Liang Peng, Xiaopei Wu, Zheng Yang, Haifeng Liu, and Deng Cai. DID-M3D: Decoupling instance depth for monocular 3D object detection. In *ECCV*, pages 71–88, 2022. x
- [66] Liang Peng, Junkai Xu, Haoran Cheng, Zheng Yang, Xiaopei Wu, Wei Qian, Wenxiao Wang, Boxi Wu, and Deng Cai. Learning occupancy for monocular 3D object detection. In *CVPR*, pages 10281–10292, 2024. 2, 3, 6, vi, vii, viii, x
- [67] Yansong Peng, Hebei Li, Peixi Wu, Yueyi Zhang, Xiaoyan Sun, and Feng Wu. D-FINE: Redefine regression task in DETRs as fine-grained distribution refinement. In *ICLR*, 2025. 3
- [68] Fanqi Pu, Yifan Wang, Jiru Deng, and Wenming Yang. MonoDGP: Monocular 3D object detection with decoupled-query and geometry-error priors. In *CVPR*, pages 6520–6530, 2025. 2, 6, 7, iv, vi, vii, viii
- [69] Yasiru Ranasinghe, Deepti Hegde, and Vishal M. Patel. MonoDiff: Monocular 3D object detection and pose estimation with diffusion models. In *CVPR*, pages 10659–10670, 2024. 1, 6, vi, vii, viii
- [70] Cody Reading, Ali Harakeh, Julia Chae, and Steven L. Waslander. Categorical depth distribution network for monocular 3D object detection. In *CVPR*, pages 8555–8564, 2021. 2, 3, vi, vii, viii, x
- [71] Shaoqing Ren, Kaiming He, Ross B. Girshick, and Jian Sun. Faster R-CNN: Towards real-time object detection with region proposal networks. In *NeurIPS*, pages 91–99, 2015. 5
- [72] Mahdi Rezaei, Mohsen Azarmi, and Farzam Mohammad Pour Mir. 3D-Net: Monocular 3D object recognition for traffic monitoring. *Expert Syst. Appl.*, 227:120253, 2023. 1
- [73] Olga Russakovsky, Jia Deng, Hao Su, Jonathan Krause, Sanjeev Satheesh, Sean Ma, Zhiheng Huang, Andrej Karpathy, Aditya Khosla, Michael S. Bernstein, Alexander C. Berg, and Li Fei-Fei. ImageNet large scale visual recognition challenge. *Int. J. Comput. Vis.*, 115(3):211–252, 2015. iv, v
- [74] Victor Sanh, Lysandre Debut, Julien Chaumond, and Thomas Wolf. DistilBERT, a distilled version of BERT: smaller, faster, cheaper and lighter. *arXiv:1910.01108 [cs.CL]*, 2019. 3
- [75] Hualian Sheng, Sijia Cai, Na Zhao, Bing Deng, Min-Jian Zhao, and Gim Hee Lee. PDR: Progressive depth regularization for monocular 3D object detection. *IEEE Trans. Circuits Syst. Video Technol.*, 33(12):7591–7603, 2023. vii, viii
- [76] Hao Shi, Chengshan Pang, Jiaming Zhang, Kailun Yang, Yuhao Wu, Huajian Ni, Yining Lin, Rainer Stiefelhagen, and Kaiwei Wang. CoBEV: Elevating roadside 3D object detection with depth and height complementarity. *IEEE Trans. Image Process.*, 33:5424–5439, 2024. 2, 7, ix
- [77] Xuepeng Shi, Zhixiang Chen, and Tae-Kyun Kim. Multivariate probabilistic monocular 3D object detection. In *WACV*, pages 4270–4279, 2023. 7, viii
- [78] Yongzhi Su, Yan Di, Guangyao Zhai, Fabian Manhardt, Jason R. Rambach, Benjamin Busam, Didier Stricker, and Federico Tombari. OPA-3D: Occlusion-aware pixel-wise aggregation for monocular 3D object detection. *IEEE Robotics Autom. Lett.*, 8(3):1327–1334, 2023. viii
- [79] Pei Sun, Henrik Kretschmar, Xerxes Dotiwalla, Aurelien Chouard, Vijaysai Patnaik, Paul Tsui, James Guo, Yin Zhou, Yuning Chai, Benjamin Caine, Vijay Vasudevan, Wei Han, et al. Scalability in perception for autonomous driving: Waymo Open Dataset. In *CVPR*, pages 2443–2451, 2020. 2, 5, 6, 7, i, ii, iii, vi, x
- [80] Mingxing Tan and Quoc V. Le. EfficientNetV2: Smaller models and faster training. In *ICML*, pages 10096–10106, 2021. iv, v
- [81] Zheng Tang, Milind Naphade, Ming-Yu Liu, Xiaodong Yang, Stan Birchfield, Shuo Wang, Ratnesh Kumar, David C. Anastasiu, and Jenq-Neng Hwang. CityFlow: A city-scale benchmark for multi-target multi-camera vehicle tracking and re-identification. In *CVPR*, pages 8797–8806, 2019. 2

- [82] Yunjie Tian, Qixiang Ye, and David S. Doermann. YOLOv12: Attention-centric real-time object detectors. *arXiv:2502.12524 [cs.CV]*, 2025. 3
- [83] Ao Wang, Hui Chen, Lihao Liu, Kai Chen, Zijia Lin, Jungong Han, and Guiguang Ding. YOLOv10: Real-time end-to-end object detection. In *NeurIPS*, pages 107984–108011, 2024. 2, 3, i, iii, iv, v, xi
- [84] Li Wang, Li Zhang, Yi Zhu, Zhi Zhang, Tong He, Mu Li, and Xiangyang Xue. Progressive coordinate transforms for monocular 3D object detection. In *NeurIPS*, pages 13364–13377, 2021. 7
- [85] Shuo Wang, Chunlong Xia, Feng Lv, and Yifeng Shi. RT-DETRv3: Real-time end-to-end object detection with hierarchical dense positive supervision. In *WACV*, pages 1628–1636, 2025. 3
- [86] Zizhang Wu, Yuanzhu Gan, Lei Wang, Guilian Chen, and Jian Pu. MonoPGC: Monocular 3D object detection with pixel geometry contexts. In *ICRA*, pages 4842–4849, 2023. viii
- [87] Zizhang Wu, Yunzhe Wu, Jian Pu, Xianzhi Li, and Xiaoquan Wang. Attention-based depth distillation with 3D-aware positional encoding for monocular 3D object detection. In *AAAI*, pages 2892–2900, 2023. 2, 3, 6, vi, vii
- [88] Zizhang Wu, Yuanzhu Gan, Yunzhe Wu, Ruihao Wang, Xiaquan Wang, and Jian Pu. FD3D: Exploiting foreground depth map for feature-supervised monocular 3D object detection. In *AAAI*, pages 6189–6197, 2024. 2, 3, 6, vi, vii
- [89] Zizhang Wu, Fan Song, Yuanzhu Gan, Yunzhe Wu, Tianhao Xu, Xiaoquan Wang, Rui Tang, and Jian Pu. Advancing 3D object detection with depth-aware spatial knowledge distillation. *IEEE Trans. Pattern Anal. Mach. Intell.*, 47(11): 10295–10310, 2025. 6, vii
- [90] Kaixin Xiong, Dingyuan Zhang, Dingkan Liang, Zhe Liu, Hongcheng Yang, Wondimu Dikubab, Jianwei Cheng, and Xiang Bai. You only look bottom-up for monocular 3D object detection. *IEEE Robot. Autom. Lett.*, 8(11):7464–7471, 2023. viii
- [91] Junkai Xu, Liang Peng, Haoran Chen, Hao Li, Wei Qian, Ke Li, Wenxiao Wang, and Deng Cai. MonoNeRD: NeRF-like representations for monocular 3D object detection. In *CVPR*, pages 6791–6801, 2023. 2, 3, 6, vi, vii, viii, x
- [92] Longfei Yan, Pei Yan, Shengzhou Xiong, Xuanyu Xiang, and Yihua Tan. MonoCD: Monocular 3D object detection with complementary depths. In *CVPR*, pages 10248–10257, 2024. 1, 2, 3, 6, 7, iii, vi, vii
- [93] Weiqing Yan, Long Xu, Hao Liu, Chang Tang, and Wujie Zhou. High-order structural relation distillation networks from LiDAR to monocular image 3D detectors. *IEEE Trans. Intell. Veh.*, 9(2):3593–3604, 2024. 2, 3, 6, vi, vii, viii
- [94] Chuanguang Yang, Zhulin An, Helong Zhou, Linhang Cai, Xiang Zhi, Jiwen Wu, Yongjun Xu, and Qian Zhang. MixSKD: Self-knowledge distillation from mixup for image recognition. In *ECCV*, pages 534–551, 2022. iv
- [95] Fan Yang, Xuan He, Wenrui Chen, Pengjie Zhou, and Zhiyong Li. MonoPSTR: Monocular 3D object detection with dynamic position and scale-aware transformer. *IEEE Trans. Instrum. Meas.*, 73:1–13, 2024. 6, vi, vii, viii
- [96] Lei Yang, Kaicheng Yu, Tao Tang, Jun Li, Kun Yuan, Li Wang, Xinyu Zhang, and Peng Chen. BEVHeight: A robust framework for vision-based roadside 3D object detection. In *CVPR*, pages 21611–21620, 2023. 7, ix
- [97] Yung-Hsu Yang, Luigi Piccinelli, Mattia Segu, Siyuan Li, Rui Huang, Yuqian Fu, Marc Pollefeys, Hermann Blum, and Zuria Bauer. 3D-MOOD: Lifting 2D to 3D for monocular open-set object detection. In *ICCV*, pages 7429–7439, 2025. 2
- [98] Hongdou Yao, Pengfei Han, Jun Chen, Zheng Wang, Yan-sheng Qiu, Xiao Wang, Yimin wang, Xiaoyu Chai, Chengloung Cao, and Wei Jin. MonOri: Orientation-guided PnP for monocular 3D object detection. *IEEE Trans. Neural Networks Learn. Syst.*, 36(10):19068–19080, 2025. viii
- [99] Xiaoqing Ye, Mao Shu, Hanyu Li, Yifeng Shi, Yingying Li, Guangjie Wang, Xiao Tan, and Errui Ding. Rope3D: The roadside perception dataset for autonomous driving and monocular 3D object detection task. In *CVPR*, pages 21309–21318, 2022. 1, 2, 5, 6, 7, 8, i, ii, iii, vi, ix, xii
- [100] Hongyi Zhang, Moustapha Cissé, Yann N. Dauphin, and David Lopez-Paz. mixup: Beyond empirical risk minimization. In *ICLR*, 2018. 2, 3, iii, viii
- [101] Jiacheng Zhang, Jiaming Li, Xiangru Lin, Wei Zhang, Xiao Tan, Junyu Han, Errui Ding, Jingdong Wang, and Guanbin Li. Decoupled pseudo-labeling for semi-supervised monocular 3D object detection. In *CVPR*, pages 16923–16932, 2024. 6, vi, vii, viii
- [102] Renrui Zhang, Han Qiu, Tai Wang, Ziyu Guo, Ziteng Cui, Yu Qiao, Hongsheng Li, and Peng Gao. MonoDETR: Depth-guided transformer for monocular 3D object detection. In *CVPR*, pages 9121–9132, 2023. 6, vi, vii
- [103] Yunpeng Zhang, Jiwen Lu, and Jie Zhou. Objects are different: Flexible monocular 3D object detection. In *CVPR*, pages 3289–3298, 2021. 7, vi, viii, ix
- [104] Yian Zhao, Wenyu Lv, Shangliang Xu, Jinman Wei, Guanzhong Wang, Qingqing Dang, Yi Liu, and Jie Chen. DETRs beat YOLOs on real-time object detection. In *CVPR*, pages 16965–16974, 2024. 3
- [105] Yi Zhou, Connelly Barnes, Jingwan Lu, Jimei Yang, and Hao Li. On the continuity of rotation representations in neural networks. In *CVPR*, pages 5745–5753, 2019. ii
- [106] Yunsong Zhou, Yuan He, Hongzi Zhu, Cheng Wang, Hongyang Li, and Qinhong Jiang. Monocular 3D object detection: An extrinsic parameter free approach. In *CVPR*, pages 7556–7566, 2021. viii
- [107] Yunsong Zhou, Hongzi Zhu, Quan Liu, Shan Chang, and Minyi Guo. MonoATT: Online monocular 3D object detection with adaptive token transformer. In *CVPR*, pages 17493–17503, 2023. vi, vii, viii
- [108] Yunsong Zhou, Quan Liu, Hongzi Zhu, Yunzhe Li, Shan Chang, and Minyi Guo. Exploiting ground depth estimation for mobile monocular 3D object detection. *IEEE Trans. Pattern Anal. Mach. Intell.*, 47(4), 2025. 2, 6, vi, vii, viii
- [109] Xiaosu Zhu, Hualian Sheng, Sijia Cai, Bing Deng, Shaopeng Yang, Qiao Liang, Ken Chen, Lianli Gao, Jingkuan Song, and Jieping Ye. RoScenes: A large-scale multi-view 3D dataset for roadside perception. In *ECCV*, pages 331–347, 2024. 2

LeAD-M3D: Leveraging Asymmetric Distillation for Real-time Monocular 3D Detection

Supplementary Material

Contents

1. Introduction

2. Related Work

- 2.1. Monocular 3D object detection
- 2.2. Knowledge distillation
- 2.3. Real-time object detection

3. Method

- 3.1. Problem statement
- 3.2. Overview
- 3.3. Asymmetric Augmentation Denoising Distillation (A2D2)
- 3.4. 3D-aware Consistent Matching (CM_{3D})
- 3.5. Confidence-Gated 3D Inference (CGI_{3D})

4. Experiments

- 4.1. Datasets and metrics
- 4.2. Comparison with lightweight M3D models
- 4.3. Comparison with SOTA M3D models
- 4.4. Ablation study
- 4.5. Qualitative results

5. Conclusion

A LeAD-M3D

- A.1. Architecture overview
- A.2. Extending the 2D baseline to 3D
- A.3. CGI_{3D} algorithm
- A.4. Implementation details

B Experiments

- B.1. Generalization of A2D2 to other baselines
- B.2. Ablation study
- B.3. Comparison with state-of-the-art methods
- B.4. Qualitative results on CM_{3D}
- B.5. Qualitative results on Rope3D

A. LeAD-M3D

A.1. Architecture overview

Our model builds on the YOLOv10 architecture [83]. We extract multi-scale features at strides 8 and 16. YOLOv10 employs dual prediction heads: a one-to-one head and a one-to-many head. During training, both heads provide supervision, which improves gradient flow and learning stabil-

Supplementary Table 8. 3D prediction heads added to YOLOv10 [83] following MonoLSS [47]. In case of KITTI [23] / Waymo [79] 12 bins and 12 residuals are learned (multi-bin). In case of Rope3D [99] the $SO(3)$ orientation matrix is learned.

Head	Output channels
2D bounding box offset head	2
2D dimension head (2D height, 2D width)	2
Projected 3D center offset head	2
3D size head (h, w, l)	3
3D depth head	1
Depth uncertainty head	1
Multi-bin orientation head	24
$SO(3)$ orientation head	6

ity. At inference time, we discard the one-to-many head and use only the one-to-one head. This design eliminates the need for NMS, which accelerates inference while maintaining a favorable accuracy–efficiency trade-off through dense training supervision.

A.2. Extending the 2D baseline to 3D

We follow best practices [47] and extend YOLOv10 with standard 3D detection heads, postprocessing pipeline, and 3D losses.

2D/3D detection heads. For clarity, we summarize the additional 3D prediction heads and their output channels in Table Tab. 8. These heads complement YOLOv10 with 3D heads and replace the original 2D-specific outputs in YOLOv10. All losses are computed per object once on the one-to-one head and up to 10 times for dense supervision on the one-to-many head. We employ the following losses:

- **Classification loss.** For classification, we use the binary cross-entropy (BCE) loss:

$$\mathcal{L}^{\text{cls}} = \sum_{n=1}^N \sum_{l=1}^2 \sum_{h_j \in H_l} \sum_{w_k \in W_l} \text{BCE}(p_{n,l,h_j,w_k}, \hat{p}_{n,l,h_j,w_k}), \quad (7)$$

where N is the batch size, W_l and H_l are the spatial dimensions at pyramid level l , $p_{n,l,h_j,w_k}^{\text{cls}}$ are ground truth probabilities, and $\hat{p}_{n,l,h_j,w_k}^{\text{cls}}$ are predicted probabilities.

- **2D offset loss.** We use L1 loss for the 2D bounding box

center offset:

$$\mathcal{L}^{\text{o2D}} = \frac{1}{\sum_n |I_n|} \sum_{n=1}^N \sum_{i \in I_n} |o_{n,i}^{\text{2D}} - \hat{o}_{n,i}^{\text{2D}}|, \quad (8)$$

where I_b denotes the instances in batch item n , $o_{n,i}^{\text{2D}}$ is the ground truth 2D bounding box offset and $\hat{o}_{n,i}^{\text{2D}}$ is the predicted 2D bounding box offset.

- **2D size loss.** We apply L1 loss to the 2D bounding box dimensions (width and height):

$$\mathcal{L}^{\text{d2D}} = \frac{1}{\sum_n |I_n|} \sum_{n=1}^N \sum_{i \in I_n} |d_{n,i}^{\text{2D}} - \hat{d}_{n,i}^{\text{2D}}|, \quad (9)$$

where $d_{n,i}^{\text{2D}}$ and $\hat{d}_{n,i}^{\text{2D}}$ are the ground truth and predicted 2D bounding box dimensions (width, height).

- **3D size loss.** We predict 3D dimensions as offsets to class-wise mean dimensions and use the following loss:

$$\mathcal{L}^{\text{d3D}} = \frac{1}{\sum_n |I_n|} \sum_{n=1}^N \sum_{i \in I_n} |d_{n,i}^{\text{3D}} - \hat{d}_{n,i}^{\text{3D}}|, \quad (10)$$

where $d_{n,i}^{\text{3D}}$ and $\hat{d}_{n,i}^{\text{3D}}$ are the ground truth and predicted 3D dimensions.

- **3D offset loss.** We use L1 loss for the projected 3D center offset:

$$\mathcal{L}^{\text{o3D}} = \frac{1}{\sum_n |I_n|} \sum_{n=1}^N \sum_{i \in I_n} |o_{n,i}^{\text{3D}} - \hat{o}_{n,i}^{\text{3D}}|, \quad (11)$$

where $o_{n,i}^{\text{3D}}$ and $\hat{o}_{n,i}^{\text{3D}}$ are the ground truth and predicted projected 3D center offsets to the anchor center.

- **Depth loss.** We use a Laplacian depth loss that incorporates predicted uncertainty $\hat{\sigma}_{b,i}$:

$$\mathcal{L}^z = \frac{1}{\sum_n |I_n|} \sum_{n=1}^N \sum_{i \in I_n} \left(\sqrt{2} \cdot \frac{|z_{n,i} - \hat{z}_{n,i}|}{\hat{\sigma}_{n,i}} + \frac{1}{2} \cdot \log \hat{\sigma}_{n,i} \right), \quad (12)$$

where $z_{n,i}$ and $\hat{z}_{n,i}$ are the ground truth and predicted depth estimates.

- **Orientation loss.** For KITTI [23] and Waymo [79], we use the multi-bin approach [62]:

$$\begin{aligned} \mathcal{L}^{\text{rot}} = & \frac{1}{\sum_n |I_n|} \sum_{n=1}^N \sum_{i \in I_n} \left[\text{CE}(\Theta_{n,i}^{\text{bin}}, \hat{\Theta}_{n,i}^{\text{bin}}) \right. \\ & \left. + \sum_{c=1}^{12} \mathbb{1}_{\Theta_{n,i,c}^{\text{bin}}=1} [|\Theta_{n,i,c}^{\text{res}} - \hat{\Theta}_{n,i,c}^{\text{res}}|] \right], \end{aligned} \quad (13)$$

where $\mathbb{1}$ is the indicator function, $\Theta_{n,i}^{\text{bin}}$ and $\hat{\Theta}_{n,i}^{\text{bin}}$ are ground truth and predicted bin probabilities, and $\Theta_{n,i,c}^{\text{res}}$ and $\hat{\Theta}_{n,i,c}^{\text{res}}$ are ground truth and predicted angle residuals.

For Rope3D [99], we predict allocentric orientation using Gram-Schmidt orthogonalization [105], following prior work [4, 60, 61]. We convert allocentric to egocentric orientation at inference:

$$\mathcal{L}^{\text{rot}} = \frac{1}{\sum_n |I_n|} \sum_{n=1}^N \sum_{i \in I_n} |R_{n,i}^{\text{alloc}} - \hat{R}_{n,i}^{\text{alloc}}|, \quad (14)$$

where $R_{n,i}^{\text{alloc}}$ and $\hat{R}_{n,i}^{\text{alloc}}$ are the ground truth and predicted allocentric $SO(3)$ orientation matrices.

- **Total loss.** The total loss presented in the main paper splits up into the following task-related losses:

$$\mathcal{L}^{\text{2D}} = \lambda^{\text{d2D}} \mathcal{L}^{\text{d2D}} + \lambda^{\text{o2D}} \mathcal{L}^{\text{o2D}} \quad (15)$$

$$\mathcal{L}^{\text{3D}} = \lambda^{\text{d3D}} \mathcal{L}^{\text{d3D}} + \lambda^{\text{o3D}} \mathcal{L}^{\text{o3D}} + \lambda^{\text{rot}} \mathcal{L}^{\text{rot}} + \lambda^z \mathcal{L}^z \quad (16)$$

We set the loss weights as follows:

$$\begin{aligned} \lambda^{\text{d2D}} &= 0.02, & \lambda^{\text{o2D}} &= 0.02, & \lambda^{\text{d3D}} &= 1.0, \\ \lambda^{\text{o3D}} &= 1.0, & \lambda^{\text{rot}} &= 1.0, & \lambda^z &= 1.0, \\ \lambda^{\text{distill}} &= 0.1. \end{aligned}$$

A.3. CGI_{3D} algorithm

In Algorithm 1 we provide the algorithmic representation of CGI_{3D} presented in the main paper.

A.4. Implementation details

Hardware and runtime evaluation. We train on a single NVIDIA RTX 8000 GPU. All runtime evaluations are also conducted on the same hardware. Latency is defined as the total execution time, measured from the start of the forward pass through the completion of all post-processing operations. This measurement includes associated CPU activity within the post-processing step, but excludes image-to-GPU data transfer. For the measurements, we perform a warmup phase followed by 1000 forward passes with batch size 1 and report the median inference time. Due to TensorRT’s numerical quantization, a slight AP variance of ± 0.2 can be observed. For TensorRT we use the following parameters: Half tensor, simplify, workspace 16GB, image size 384×1280 and batch size 1.

Training configuration. We use gradient accumulation to simulate a virtual batch size of 64. We apply the Adam optimizer [37] with an initial learning rate of 0.001, weight decay of 0.0005, and 3 warmup epochs. We use cosine annealing as the learning rate scheduler. For distillation, we use the features from the one-to-one head as targets for both student heads. We empirically observe that the L model architecture of YOLOv10-M3D offers no benefit over the B model despite the larger capacity. We therefore

Algorithm 1 Confidence-Gated 3D Inference (CGI_{3D})

Require: Neck features $\mathcal{F}^{(8)}, \mathcal{F}^{(16)}$; heads f_{cls}, f_{2d}, f_{3d} ; top- k value k

Ensure: Local 2D/3D predictions at selected multi-scale locations

- 1: $P^{(8)} \leftarrow f_{cls}(\mathcal{F}^{(8)})$ ▷ dense class scores on stride-8 grid
 - 2: $P^{(16)} \leftarrow f_{cls}(\mathcal{F}^{(16)})$ ▷ dense class scores on stride-16 grid
 - 3: $[S, \text{lvl}, \text{coord}] \leftarrow \text{TaggedConcat}(\text{Flatten}(P^{(8)}), \text{Flatten}(P^{(16)}))$ ▷ concatenate scores; keep origin level (8/16) and coordinates
 - 4: $J \leftarrow \text{TopKIndices}(S, k)$ ▷ indices into concatenated scores
 - 5: $\text{centers} \leftarrow (\text{lvl}[J], \text{coord}[J])$ ▷ selected centers with FPN tags
 - 6: $Q \leftarrow \text{Extract3x3}(\mathcal{F}^{(8)}, \mathcal{F}^{(16)}, \text{Nbr}_{3 \times 3}(\text{centers}))$ ▷ gather all 3×3 patches from their respective FPN maps
 - 7: $b^{2D} \leftarrow f_{2d}(Q)$ ▷ compute 2D outputs for gathered patches
 - 8: $b^{3D} \leftarrow f_{3d}(Q)$ ▷ compute 3D outputs for gathered patches
 - 9: **return** $b^{2D}, b^{3D}, S[J]$
-

exclude the L model from our experiments. CM_{3D} replaces the prediction-to-ground truth scoring of YOLOv10-M3D. Other matching criteria (*e.g.* maximum anchor radius) of YOLOv10 [83] are kept.

Data augmentation. We apply the following augmentations during training: horizontal flipping with probability 0.5, random cropping with probability 0.5, translation augmentation with a maximum shift of 0.1 times the image size, scaling with resize factors between 0.6 and 1.4, and mixup with probability of 0.5 and a blending ratio of 0.5 (following previous work[47, 60]). We empirically observe that the overall accuracy is relatively robust to modest changes of the mixup probabilities and blending ratios; for simplicity, we keep both at 0.5.

Dataset-specific settings. On KITTI [23], we train both teacher and student for 400 epochs each. On Rope3D [99], we train for 100 epochs. On Waymo [79], we train for 45 epochs. For Waymo [79] and Rope3D[99], we use 50% of the original image resolution to accelerate experiments. We follow GroundMix [60] and learn virtual depth for Rope3D[99], as it contains images with varying intrinsic parameters.

Hyperparameters. For CM_{3D}, we set $\alpha = 0.5$, $\beta = 1.0$, and $\gamma = 1.0$. Our baseline and LeAD-M3D follows the 2D detector YOLOv10 [83] and outputs the top- k predictions during inference. For top- k selection in CGI_{3D}, we use $k = 50$ for KITTI and Waymo, and $k = 200$ for Rope3D. As all methods use a top- k based selection by default, an enabled CGI_{3D} produces the same predictions as if it were deactivated.

B. Experiments

B.1. Generalization of A2D2 to other baselines

To demonstrate the generality of our A2D2 approach, we integrate it into two other popular M3D methods, MonoLSS [47] and MonoCD [92], and report the results in Supplementary Tab. 9.

Supplementary Table 9. **Ablation study on the effectiveness of A2D2 on different baseline detectors.** Results are shown for cars on the KITTI [23] validation set.

Method	AP ^{0.7} _{3D R40} Car ↑		
	Easy	Mod.	Hard
MonoLSS [47]	25.91	18.29	15.94
MonoLSS [47] + A2D2	27.53	20.05	16.99
<i>Impr.</i>	<i>+1.62</i>	<i>+1.76</i>	<i>+1.05</i>
MonoCD [92]	24.22	18.27	15.42
MonoCD [92] + A2D2	28.30	21.00	18.56
<i>Impr.</i>	<i>+4.08</i>	<i>+2.73</i>	<i>+3.14</i>

Since these methods employ different 2D detection architectures, we retain their original label-assignment strategies and do not apply our CM_{3D}. Furthermore, as both models only offer a single standard size, we first train them conventionally and then use the resulting model as a self-distillation teacher for our method.

Despite these architectural differences and constraints, we observe consistent performance gains across all evaluation metrics. This confirms that our mixup [100]-based denoising distillation effectively transfers and provides benefits to diverse baseline architectures.

B.2. Ablation study

A2D2 ablation. In Supplementary Tab. 10, we complement the A2D2 ablation study in the main paper. We use AP Moderate as the primary metric. Replacing the relative depth error with absolute depth error for the teacher-quality weight reduces AP by 0.42. We hypothesize this overemphasizes near-range objects (with naturally smaller absolute residuals), which skews the data distribution and thereby harms generalization.

Replacing our sophisticated distillation pipeline with vanilla distillation (*i.e.*, without importance and quality weighting, using backbone instead of depth feature for dis-

Supplementary Table 10. **Detailed ablation study on A2D2.** We report $AP_{3D|R40}^{0.7}$ for cars on the KITTI [23] validation set using the B model. Results are sorted by Mod. accuracy.

Method	Easy \uparrow	Mod. \uparrow	Hard \uparrow
LeAD-M3D B (Ours)	28.33	22.72	19.98
Ours w/ absolute quality ind.	<u>28.03</u>	<u>22.30</u>	<u>19.68</u>
Ours w/ online self-distillation	27.45	21.80	19.57
Ours w/ simple distillation	26.10	20.50	17.73
Ours w/ MixSKD [94]	25.14	19.68	18.22
Ours w/o A2D2	26.26	20.43	17.71


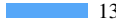

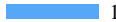

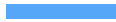
tillation, and without the asymmetric augmentation) leads to a substantial drop of 2.22 AP and only a minimal gain of 0.07 AP vs. not applying knowledge distillation at all. This highlights the crucial role of our bespoke distillation components. We hypothesize this minimal improvement occurs because, without the quality weighting, the student only benefits from the difference in model capacity; however, the B and X models tend to perform similarly (*cf.* Supplementary Tab. 16), leading to negligible gains.

Finally, we evaluate replacing our distillation strategy with MixSKD [94]. This substitution results in the largest performance drop of 3.04 AP, an expected result. MixSKD is primarily designed for classification tasks, whereas our distillation approach (A2D2) was specifically engineered for the geometric and structured nature of M3D. To clarify this significant performance gap, we provide a detailed comparison highlighting the core methodological differences that explain the observed 3.04 AP drop:

- MixSKD is tailored for image classification tasks, whereas our method is designed for M3D. As a result, MixSKD distills classification or backbone features, whereas our approach focuses on distilling depth features.
- MixSKD performs distillation across all spatial features. This means, in case of MixSKD most of the distillation happens for background rather than foreground features. In contrast, A2D2 distills instance-specific features only.
- MixSKD relies on interpolated features for distillation, whereas our framework distills teacher features.
- MixSKD performs online self-distillation, while we perform offline distillation (*cf.* A2D2 ablation in the main paper).
- We employ quality and importance weighting to focus distillation on valuable teacher knowledge, a component absent in MixSKD.
- Beyond the core feature distillation loss, MixSKD requires additional components, including a discriminator head, distinct auxiliary branches, and multiple logit distillation losses. In contrast, our method outperforms it with a simpler design relying solely on a single feature

distillation loss.

Supplementary Table 11. **Comparison of detection accuracy with and without pretrained weights for different methods on the KITTI [23] validation set.** *P*: Indicates, whether pretrained weights are used (MonoLSS [47], MonoDGP [68]: ImageNet [73], LeAD-M3D X: MS-COCO [50]).

Method	P	$AP_{3D R40}^{0.7}$	Mod. Car \uparrow
MonoDGP [68]	✓		22.34
MonoDGP [68]	✗		13.93 -37.6%
MonoLSS [47]	✓		18.29
MonoLSS [47]	✗		15.85 -13.3%
LeAD-M3D X (Ours)	✓		22.94
LeAD-M3D X (Ours)	✗		19.21 -16.3%

Effect of pretrained weights. Most monocular 3D methods initialize with ImageNet [73] pretrained weights. For YOLOv10, only MS-COCO [50] pretrained weights are publicly available. We therefore adopt MS-COCO initialization. MS-COCO provides denser 2D bounding box supervision than ImageNet, though the dataset is over 100 times smaller. To assess the impact of pretraining, we compare accuracy with and without pretrained weights across LeAD-M3D and other SOTA methods [47, 68] in Supplementary Tab. 11. Notably, without pretraining, our accuracy remains higher than MonoLSS [47] with pretraining. The relative drops of 13.3% and 16.3% are similar, indicating stable learning. In contrast, MonoDGP [68] suffers a 37.6% drop without pretraining. We hypothesize this instability stems from attention layers, which require more extensive pretraining. We conclude that our approach is robust to pretraining and that MS-COCO weights provide no inherent advantage.

Backbone ablation. In Supplementary Tab. 12, we perform an ablation study on the feature extractor by replacing the standard YOLOv10 [83] backbone with the EfficientNetV2 [80] (ENV2) series. These ENV2 models are initialized using ImageNet [73] pretrained weights only, ensuring no 2D supervision was involved. Following our standard distillation procedure, we train the largest variant (ENV2-L) as the teacher, distilling knowledge to student models L, M, and S. We observe consistent accuracy improvements over the baseline, with two of the three ENV2 models achieving even higher detection accuracy than LeAD-M3D X. This superior accuracy is also confirmed for the test set in Supplementary Tab. 13, where the ENV2 L backbone outperforms the YOLOv10 X backbone in 5 out of 6 metrics. Yet, the computational cost is higher for the ENV2 backbone. Due to this efficiency trade-off, we retain the

Supplementary Table 12. **Detection accuracy for different backbones on the KITTI [23] validation set.** We compare the YOLOv10 [83] backbones (MS-COCO [50] pretrained) with EfficientNetV2 [80] backbones (ImageNet [73] pretrained). **Time:** Inference time for batch size 1 without TensorRT (hardware: NVIDIA RTX 8000).

Method	Backbone	Time ↓	AP ↑
LeAD-M3D	YOLOv10 [83] N	9.7	18.41
LeAD-M3D	YOLOv10 [83] S	10.2	20.65
LeAD-M3D	YOLOv10 [83] M	13.3	22.34
LeAD-M3D	YOLOv10 [83] B	13.9	22.72
LeAD-M3D	YOLOv10 [83] X	23.6	22.94
YOLOv10-M3D	EfficientNetV2 [80] S	32.5	19.76
LeAD-M3D	EfficientNetV2 [80] S	24.8	22.70
YOLOv10-M3D	EfficientNetV2 [80] M	41.2	19.86
LeAD-M3D	EfficientNetV2 [80] M	31.6	23.36
YOLOv10-M3D	EfficientNetV2 [80] L	58.5	19.99
LeAD-M3D	EfficientNetV2 [80] L	51.4	23.64

Supplementary Table 13. **Detection accuracy on the KITTI[23] test set.** LeAD-M3D with EfficientNetV2 [80] (ENV2) weights outperforms YOLOv10-M3D X and MonoTAKD [51] in 5 out of 6 metrics. Notice that our approach runs more than five times faster than MonoTAKD [51] and requires no LiDAR input.

Method	AP ^{0.7} _{3D/R40} ↑			AP ^{0.7} _{BEV/R40} ↑		
	Easy	Mod.	Hard	Easy	Mod.	Hard
MonoTAKD [51]	27.91	19.43	16.51	38.75	27.76	24.14
LeAD-M3D X	30.76	21.20	18.76	38.33	26.57	23.74
LeAD-M3D w/ ENV2 [80] L	31.18	20.86	19.10	39.74	27.35	24.43

Supplementary Table 14. **Runtime Comparison between YOLOv10-M3D N (Baseline) and LeAD-M3D N (Ours) on the KITTI [23] validation set.** Our method consistently achieves a significantly faster runtime across all tested devices compared to the baseline. CPU inference uses the Intel Xeon Gold 6254 and GPU inference uses the NVIDIA RTX 8000.

Method	Baseline ↓	Ours ↓	Change
CPU	541.7 ms	243.4 ms	- 55 %
GPU	16.2 ms	9.7 ms	- 40 %
GPU w/ TensorRT	1.9 ms	1.4 ms	- 26 %

YOLOv10 [83] architecture as the standard backbone for our main experiments.

Runtime comparison across devices. In Supplementary Tab. 14, we comprehensively compare the inference latency of our proposed LeAD-M3D N against the baseline YOLOv10-M3D N across CPU, standard GPU, and TensorRT environments. Our head-level modifications yield substantial speed ups across all platforms: 55% on the

Supplementary Table 15. **Runtime decomposition of the different model components.** CGI_{3D} saves significant computation time at the 2D/3D regression heads. We evaluate the design choices on the KITTI [23] validation set using the N model. All runtimes are evaluated with an NVIDIA RTX8000 and without exporting to TensorRT.

Component	Baseline ↓	Ours ↓	Change
Backbone	8.17 ms	8.18 ms	+ 0.01 ms
Classification head	0.41 ms	0.41 ms	- 0.00 ms
Patch extraction	—	0.26 ms	+ 0.26 ms
2D/3D regression heads	7.37 ms	0.58 ms	- 6.79 ms
Decoding	0.22 ms	0.28 ms	+ 0.06 ms
Total head	8.00 ms	1.53 ms	- 6.47 ms
Total	16.17 ms	9.71 ms	- 6.46 ms

CPU and 40% on the standard GPU, confirming benefits in compute-bound regimes. Critically, the speed up decreases to 26% in the sub-2ms TensorRT environment. This clear dependency demonstrates the transition to an overhead-bound state in highly optimized hardware, where fixed costs (*e.g.*, kernel launch latency) dominate the total runtime and thus limit the realized benefit of computational savings. Furthermore, in terms of memory footprint, LeAD-M3D N demonstrates superior efficiency, requiring a peak memory of 169.4MB and reserved memory of 224.4MB, compared to 211.2MB (peak) and 249.6MB (reserved) for YOLOv10-M3D N, respectively.

Runtime decomposition. In Supplementary Tab. 15, we present a detailed runtime decomposition of LeAD-M3D N against YOLOv10-M3D N, complementing the high-level total runtime results. Specifically, while the CGI_{3D} patch extraction introduces a minor 0.26 ms overhead, it enables a substantial 92% reduction in the 2D/3D head’s computational cost. For this patch extraction, we evaluated a custom CUDA kernel but found that simple indexing proved equally efficient; we therefore adopt the simpler implementation. The minor variations observed in the backbone and decoding runtimes are attributed to standard measurement noise.

B.3. Comparison with state-of-the-art methods

KITTI [23] validation set. Supplementary Tab. 16 compares LeAD-M3D with other methods on the KITTI [23] validation set. LeAD-M3D X achieves the highest accuracy among all variants and offers the best accuracy-to-runtime trade-off. We also observe consistent gains across all model sizes compared to our baseline, confirming the effectiveness of our proposed components.

KITTI [23] test set. Supplementary Tab. 17 provides the comprehensive KITTI [23] test results for the car category,

Supplementary Table 16. **Comparison with SOTA monocular methods on the KITTI [23] validation set for the car category (IoU=0.7, R40).** *Extra* highlights methods that utilize auxiliary data during training to improve accuracy. *Time*: For a fair comparison, inference time is shown in ms for batch size 1 without TensorRT (hardware: NVIDIA RTX 8000). [†] As no code is available, we report the author’s reported runtime, if it is available. **AP**: Moderate accuracy is shown.

Method	Extra	Time ↓	AP ^{0.7} _{3D R40} ↑
MonoDistill [16]	LiDAR	46.7	16.03
ADD [87]	LiDAR	— [†]	16.81
MonoNeRD [91]	LiDAR	1380.3	19.96
HSRDN [93]	LiDAR	— [†]	13.61
MonoFG [22]	LiDAR	56 [†]	16.46
MonoSTL [18]	LiDAR	25.7	17.14
MonoSGC [32]	LiDAR	35.0	19.55
OccupancyM3D [66]	LiDAR	213.9	19.96
DPL _{FLEX} [101]	Unlabeled	28.9	19.84
MonoSG [19]	Stereo	36 [†]	20.77
MonoTAKD [51]	LiDAR	270.1	22.61
<hr/>			
HomoLoss [25]	Geometry	28.9 [†]	16.89
MonoDDE [45]	Geometry	36 [†]	19.75
MonoATT [107]	Geometry	56 [†]	22.47
MonoUNI [33]	Geometry	23.2	16.73
MonoCD [92]	Geometry	28.1	19.37
DA3D [34]	Geometry	24.1	21.68
MoGDE [108]	Geometry	— [†]	20.35
MonoDGP [68]	Geometry	68.1	22.34
<hr/>			
MonoCon [52]	—	15.5	19.01
MonoDETR [102]	—	47.8	16.47
DDML [15]	—	15.5	19.43
MonoPSTR [95]	—	35.0	17.01
FD3D [88]	—	40 [†]	20.23
MonoLSS [47]	—	20.2	18.29
MonoDiff [69]	—	86 [†]	22.02
MonoMAE [35]	—	38 [†]	20.90
<hr/>			
YOLOv10-M3D N (Baseline)	—	16.2	14.52
LeAD-M3D N (Ours)	—	9.7	18.41
<hr/>			
YOLOv10-M3D S (Baseline)	—	16.7	17.85
LeAD-M3D S (Ours)	—	10.2	20.65
<hr/>			
YOLOv10-M3D M (Baseline)	—	21.0	19.26
LeAD-M3D M (Ours)	—	13.3	22.34
<hr/>			
YOLOv10-M3D B (Baseline)	—	21.5	19.60
LeAD-M3D B (Ours)	—	13.9	22.72
<hr/>			
YOLOv10-M3D X (Baseline)	—	31.7	19.98
LeAD-M3D X (Ours)	—	23.6	22.94

serving as a detailed appendix to the main paper summaries. LeAD-M3D obtains the highest score on the primary metric, AP^{0.7}_{3D|R40}, demonstrating strong geometric accuracy. In contrast, MonoTAKD [51] reports higher numbers on AP^{0.7}_{BEV|R40}. We attribute this outcome to the inherent design difference: AP^{0.7}_{BEV|R40} is tightly coupled to raw depth quality, a task where MonoTAKD gains a significant advantage by being trained with additional dense LiDAR depth

supervision. This extra data modality simplifies depth prediction and inflates depth-error sensitive metrics. More importantly, MonoTAKD’s dependency on compute-intensive 3D volume processing results in an inference speed that is more than an order of magnitude slower than ours. As shown in Supplementary Tab. 13, when utilizing a different backbone, such as EfficientNetv2, LeAD-M3D outperforms MonoTAKD [51] in five out of six metrics while maintaining a runtime over 5x faster and training purely on image data.

While the car category is the primary focus on KITTI, we also evaluate on pedestrian and cyclist categories. Supplementary Tab. 18 reports average accuracy across all three categories. Our two largest models achieve the highest average accuracy among methods that do not use extra training data.

While MonoLSS [47] achieves higher accuracy on the pedestrian category, we hypothesize this is due to their Learnable Sample Selection (LSS) module. This module lets the model shift the focus of the heads to meaningful areas of the feature map, which might be particularly relevant for the elongated pedestrian bounding boxes. However, its overall average precision is still significantly lower than ours.

Among methods with extra data, only MonoTAKD [51] surpasses our average accuracy. While our car and pedestrian accuracy is higher, MonoTAKD achieves a higher cyclist accuracy. We hypothesize this is due to additional LiDAR supervision, which provides denser training signals for the cyclist category. This category is extremely under-represented in KITTI, making extra supervision more valuable.

Rope3D [99]. Supplementary Tab. 19 provides the complete Rope3D [99] performance table. The results are consistent with those shown in the main paper, further confirming our method’s effectiveness across diverse datasets and viewpoints. MonoFlex [103] achieves higher accuracy on the big vehicle class when supplied with ground-plane inputs; however, its Big Vehicle accuracy degrades by −92.6% AP^{0.7}_{3D} when ground-plane inputs are unavailable.

Waymo [79]. Supplementary Tab. 20 presents the full Waymo [79] results, comparing the baseline with our approach. These results are obtained using the training and validation split defined by DEVIANT [39].

The DEVIANT [39] vs. CaDDN [70] Waymo protocols. The original Waymo dataset is a multi-view benchmark. CaDDN [70] adapted it for M3D by using every third frame for training and filtering objects not visible in the front-view camera. Since then, two primary versions have emerged:

Supplementary Table 17. **Comparison with SOTA monocular methods on the KITTI [23] test set for the car category.** *Extra* highlights methods that utilize auxiliary data during training to improve accuracy. *Params*: Million model parameters. *GFLOPs*: Giga FLOPs per image. *Time*: For a fair comparison, inference time is shown in ms for batch size 1 without TensorRT (hardware: NVIDIA RTX 8000). We highlight the best performing methods among the methods without geometric assumptions and without extra training data. [†] With no code available, we present the author’s stated runtime, where provided.

Method	Venue	Extra	Params ↓	GFLOPs ↓	Time ↓	AP ^{0.7} _{3D R40} ↑			AP ^{0.7} _{BEV R40} ↑		
						Easy	Mod.	Hard	Easy	Mod.	Hard
MonoDistill [16]	ICLR 22	LiDAR	50.1	159	46.7	22.97	16.03	13.60	31.87	22.59	19.72
ADD [87]	AAAI 23	LiDAR	—	—	— [†]	25.61	16.81	13.79	35.20	23.58	20.08
MonoNeRD [91]	CVPR 23	LiDAR	6.6	4220	1380.3	22.75	17.13	15.63	31.13	23.46	20.97
HSRDN [93]	TIV 24	LiDAR	—	—	— [†]	26.37	16.39	14.22	36.49	23.96	19.67
MonoFG [22]	ACM 24	LiDAR	—	—	56 [†]	24.35	16.46	13.84	32.42	21.64	18.60
MonoSTL [18]	TCSVT 24	LiDAR	50.0	159	25.7	25.33	16.13	13.35	33.87	22.42	19.04
MonoDSSMs-A	ACCV 24	LiDAR	23.6	—	28.8 [†]	21.47	14.55	11.78	28.84	19.54	16.30
MonoSGC [32]	TIV 24	LiDAR	23.1	173	35.0	27.01	16.77	14.61	35.78	23.27	19.92
OccupancyM3D [66]	CVPR 24	LiDAR	28.3	389	213.9	25.55	17.02	14.79	35.38	24.18	21.37
DPL _{FLX} [101]	CVPR 24	Unlabeled	21.5	152	28.9	24.19	16.67	13.83	33.16	22.12	18.74
MonoSG [19]	RAL 25	Stereo	—	—	36 [†]	25.77	16.70	14.22	33.46	22.12	19.16
DK3D [89]	TPAMI 25	LiDAR	19.6	—	30.1 [†]	25.63	16.82	13.81	35.23	23.59	20.10
MonoTAKD [51]	CVPR 25	LiDAR	46.9	810	270.1	27.91	19.43	16.51	38.75	27.76	24.14
HomoLoss	CVPR 22	Geometry	21.5	152	28.9	21.75	14.94	13.07	29.60	20.68	17.81
MonoDDE	CVPR 22	Geometry	—	—	36 [†]	25.53	16.59	14.53	33.41	22.81	19.57
PDR [75]	TCSVT 23	Geometry	—	—	29 [†]	23.69	16.14	13.78	—	—	—
MonoATT [107]	CVPR 23	Geometry	—	—	56 [†]	24.72	17.37	15.00	36.87	24.42	21.88
MonoUNI [33]	NeurIPS 23	Geometry	22.7	122	23.2	24.75	16.73	13.49	33.28	23.05	16.39
DA3D [34]	TIM24	Geometry	20.1	93	24.1	27.76	20.47	17.89	36.83	26.92	23.41
MonoCD [92]	CVPR 24	Geometry	21.8	171	28.1	25.53	16.59	14.53	33.41	22.81	19.57
MoGDE [108]	TPAMI 25	Geometry	—	—	— [†]	27.25	17.93	15.80	38.84	26.02	23.27
MonoDGP [68]	CVPR 25	Geometry	43.3	276	68.1	26.35	18.72	15.97	35.24	25.23	22.02
MonoCon [52]	AAAI22	—	19.6	115	15.5	22.50	16.46	13.95	31.12	22.10	19.00
Cube R-CNN [4]	CVPR 23	—	47.2	142	27.3	23.59	15.01	12.56	31.70	21.20	18.43
MonoDETR [102]	ICCV 23	—	37.7	119	47.8	25.00	16.47	16.38	33.60	22.11	18.60
DDML [15]	NeurIPS 23	—	19.6	115	15.5	23.31	16.36	13.73	—	—	—
MonoPSTR [95]	TIM 24	—	38.0	96	35.0	26.15	17.01	13.70	34.79	22.88	19.40
FD3D [88]	AAAI 24	—	—	—	40 [†]	25.38	17.12	14.50	34.20	23.72	20.76
MonoLSS [47]	3DV 24	—	21.5	127	20.2	26.11	19.15	16.94	34.89	25.95	22.59
MonoDiff [69]	CVPR 24	—	—	—	86 [†]	30.18	21.02	18.16	—	—	—
MonoMAE [35]	NeurIPS 24	—	—	—	38 [†]	25.60	18.84	16.78	34.14	24.93	21.76
GATE3D [31]	CVPRW 25	—	—	—	82 [†]	26.07	18.85	16.76	33.94	25.06	22.04
LeAD-M3D N	(Ours)	—	3.8	14	9.7	24.31	16.49	14.14	32.22	21.72	19.41
LeAD-M3D S	(Ours)	—	10.1	38	10.2	27.28	18.87	16.37	34.86	24.17	21.32
LeAD-M3D M	(Ours)	—	19.7	88	13.3	28.08	19.47	17.66	36.21	25.46	22.89
LeAD-M3D B	(Ours)	—	24.9	133	13.9	29.10	20.17	18.34	37.65	26.63	23.75
LeAD-M3D X	(Ours)	—	36.3	218	23.6	30.76	21.20	18.76	38.33	26.57	23.74

- The original CaDDN version applies the same initial object filtering to both the training and validation sets.
- The alternative DEVIANT [39] version is more restrictive. It additionally removes objects whose projected 3D centers fall outside the image from the training set, but retains them in the validation set.

The DEVIANT version has become more common in recent literature. We therefore adopt it for our main experiments (*cf.* the main paper and Supplementary Tab. 20).

For completeness, we also provide results on the CaDDN version in Supplementary Tab. 21. LeAD-M3D X achieves

the highest accuracy while being 2 to 43 times faster than existing methods. Our analysis of prior work reveals that the primary computational bottlenecks in methods like OccupancyM3D [66], MonoNeRD [91], CaDDN [70], and CMKD [28] stem from two key stages: lifting the 2D image to a 3D volume and the subsequent 3D volume processing. Specifically, CaDDN [70] faces an additional drag due to the use of computationally intensive fully connected layers for depth estimation.

Supplementary Table 18. **Performance comparison with SOTA M3D methods on the KITTI [23] test set.** *Extra* highlights methods that utilize auxiliary data during training to improve accuracy. We highlight the best performing methods among the methods without geometric assumptions and without extra training data.

Method	Extra	Car. AP ^{0.7} _{3D R40} ↑			Ped. AP ^{0.5} _{3D R40} ↑			Cyclist AP ^{0.5} _{3D R40} ↑			Average AP _{3D R40} ↑		
		Easy	Mod.	Hard	Easy	Mod.	Hard	Easy	Mod.	Hard	Easy	Mod.	Hard
CMKD [28]	LiDAR	25.09	16.99	15.30	17.79	11.69	10.09	9.60	5.24	4.50	17.49	11.37	9.96
MonoRun [6]	LiDAR	19.65	12.30	10.58	10.88	6.78	5.83	1.01	0.61	0.48	10.51	6.56	5.63
CaDDN [70]	LiDAR	19.17	13.41	11.46	12.87	8.14	6.76	7.00	3.41	3.30	13.01	8.32	7.17
DD3D [64]	LiDAR	23.22	16.34	14.20	13.91	9.30	8.05	2.39	1.52	1.31	13.17	8.64	7.85
AutoShape [54]	Shapes	22.47	14.17	11.36	5.46	3.74	3.03	5.99	3.06	2.70	11.31	6.99	5.70
MonoEF [106]	Odometry	21.29	13.87	11.71	4.27	2.79	2.21	1.80	0.92	0.71	9.12	5.86	4.88
MonoDistill [16]	LiDAR	24.31	18.47	15.76	12.79	8.17	3.39	5.53	2.81	2.40	14.21	9.82	7.18
MonoJSG [49]	LiDAR	24.69	16.14	13.64	11.02	7.49	6.41	5.45	3.21	2.57	13.72	8.95	7.54
DCD [43]	Shapes	23.81	15.90	13.21	10.37	6.73	6.28	4.72	2.74	2.41	12.97	8.31	7.30
Pseudo-Stereo [12]	LiDAR	23.74	17.74	15.14	16.95	10.82	9.26	11.22	6.18	5.21	17.30	11.58	9.87
MonoPGC [86]	LiDAR	24.68	17.17	14.14	14.16	9.67	8.26	5.88	3.30	2.85	14.91	10.05	8.42
MonoNeRD [91]	LiDAR	22.75	17.13	15.63	13.20	8.26	7.02	4.79	2.48	2.16	13.58	8.88	8.27
OPA-3D [78]	LiDAR	24.60	17.05	14.25	16.64	11.04	9.38	7.52	4.79	4.22	16.25	11.23	9.28
HSRDN [93]	LiDAR	26.37	16.39	14.22	14.35	9.90	8.71	13.29	6.85	6.24	18.00	11.04	9.72
OccupancyM3D [66]	LiDAR	25.55	17.02	14.79	14.68	9.15	7.80	7.37	3.56	2.84	15.87	9.91	8.48
DPL _{FLEX} [101]	Unlabeled	24.19	16.67	13.83	11.66	7.52	6.16	8.41	4.51	3.59	14.75	9.57	7.86
MonOri [98]	LiDAR	25.20	16.77	14.45	18.97	12.76	11.00	9.47	5.87	5.35	17.88	11.80	10.27
MonoSG [19]	Stereo	25.77	16.70	14.22	14.72	9.53	7.87	4.18	2.65	2.09	16.12	9.62	8.06
MonoTAKD [51]	LiDAR	27.91	19.43	16.51	16.15	10.41	9.68	13.54	7.23	6.86	19.20	12.36	11.01
<hr/>													
MonoPair [11]	Geometry	13.04	9.99	8.65	10.02	6.68	5.53	3.79	2.12	1.83	8.95	6.26	4.79
GUPNet [55]	Geometry	20.11	14.20	11.77	14.95	9.76	8.41	5.58	3.21	2.66	13.55	9.06	7.61
MonoFlex [103]	Geometry	19.94	13.89	12.07	9.43	6.31	5.26	4.17	2.35	2.04	11.18	7.52	6.46
MonoDDE [45]	Geometry	24.93	17.14	15.10	11.13	7.32	6.67	5.94	3.78	3.33	13.45	9.41	8.37
DEVIANT [39]	Geometry	21.88	14.46	11.89	13.43	8.65	7.69	5.05	3.13	2.59	14.45	8.75	7.39
HomoLoss [25]	Geometry	21.75	14.94	13.07	11.87	7.66	6.82	5.48	3.50	2.99	13.03	8.70	7.62
YOLOBU [90]	Geometry	22.43	16.21	13.73	11.68	7.58	6.22	5.25	2.83	2.31	13.12	8.87	7.42
MonoRCNN++ [77]	Geometry	20.08	13.72	11.34	12.26	7.90	6.62	3.17	1.81	1.75	11.84	7.81	6.88
SSD-MonoDETR [26]	Geometry	24.52	17.88	15.69	12.64	9.88	8.58	7.79	5.76	4.33	14.98	11.17	9.53
PDR [75]	Geometry	23.69	16.14	13.78	11.61	7.72	6.40	2.72	1.57	1.50	12.67	9.77	7.23
MonoATT [107]	Geometry	24.72	17.37	15.00	13.20	8.26	7.02	4.79	2.48	2.16	14.23	9.37	8.06
MonoUNI [33]	Geometry	24.75	16.73	13.49	15.78	10.34	8.74	7.34	4.28	3.78	15.96	10.45	8.67
DA3D [34]	Geometry	27.76	20.47	17.89	4.62	2.95	2.58	3.37	1.86	1.48	11.92	8.43	7.32
MoGDE [108]	Geometry	27.25	17.93	15.80	11.27	8.33	7.67	7.02	3.96	3.41	15.18	10.07	8.96
MonoDGP [68]	Geometry	26.35	18.72	15.97	15.04	9.89	8.38	5.28	2.82	2.65	15.56	10.48	9.00
<hr/>													
MonoCon [52]	—	22.50	16.46	13.95	13.10	8.41	6.94	2.80	1.92	1.55	12.80	8.93	7.33
MonoDTR [30]	—	24.52	18.57	15.51	15.33	10.18	8.61	5.05	3.27	3.19	14.97	10.67	9.10
Cube R-CNN [4]	—	23.59	15.01	12.56	11.17	6.95	5.87	3.65	2.67	2.28	12.80	8.21	6.90
DDML [15]	—	23.31	16.36	13.73	14.90	10.28	8.70	5.38	2.89	2.83	14.53	9.84	8.42
MonoPSTR [95]	—	26.15	17.01	13.70	13.26	8.84	6.99	7.11	4.75	4.21	15.51	10.20	8.30
MonoLSS [47]	—	26.11	19.15	16.94	17.09	11.27	10.00	7.23	4.34	3.92	16.81	11.59	10.29
MonoDiff [69]	—	30.18	21.02	18.16	13.51	8.94	7.28	8.52	5.55	4.35	17.40	11.84	9.93
MonoMM [21]	—	21.13	15.67	12.97	14.86	9.95	8.34	6.82	3.82	3.75	14.27	9.81	8.35
GATE3D [31]	—	26.07	18.85	16.76	16.25	10.53	8.91	—	—	—	—	—	—
<hr/>													
LeAD-M3D N (Ours)	—	24.31	16.49	14.14	12.78	8.18	6.80	6.11	3.34	3.10	14.40	9.34	8.01
LeAD-M3D S (Ours)	—	27.28	18.87	16.37	15.91	9.95	8.44	4.61	2.38	2.40	15.93	10.40	9.07
LeAD-M3D M (Ours)	—	28.08	19.47	17.66	15.91	10.15	8.62	8.95	5.02	4.53	17.65	11.55	10.27
LeAD-M3D B (Ours)	—	29.10	20.17	18.34	16.03	10.47	8.91	10.11	6.05	5.11	18.44	12.23	10.79
LeAD-M3D X (Ours)	—	30.76	21.20	18.76	16.68	10.98	9.20	9.28	5.48	4.70	18.91	12.55	10.89

B.4. Qualitative results on CM_{3D}

Supplementary Fig. 6 compares the prediction-to-ground truth assignments between the baseline and our proposed CM_{3D}. Using a one-to-one assignment, which is also utilized during inference, CM_{3D} achieves better object match-

ing, which we attribute to two main advantages: (1) It effectively solves misassignments that occur in crowded or mixup [100]-augmented scenes, where 2D boxes overlap heavily. Our CM_{3D} strategy resolves this confusion by considering both 2D and 3D overlap for reliable assignments.

Supplementary Table 19. **Comparison with SOTA monocular methods on the Rope3D heterologous benchmark [99].** *Extra* highlights methods that utilize auxiliary data during training to improve accuracy. *AP* denotes $AP_{3D|R40}$. *R* denotes the Rope Score [99].

Method	Extra	IoU = 0.5 \uparrow				IoU = 0.7 \uparrow			
		Car		Big Vehicle		Car		Big Vehicle	
		AP	Rope	AP	Rope	AP	Rope	AP	Rope
M3D-RPN [2]	Ground plane	36.33	48.16	24.39	37.81	11.09	28.17	3.39	21.01
MonoDLE [58]	Ground plane	31.33	43.68	23.81	36.21	12.16	28.39	3.02	19.96
MonoFlex [103]	Ground plane	37.27	48.58	47.52	55.86	11.24	27.79	13.10	28.22
BEVHeight [96]	Ground plane	29.65	42.48	13.13	28.08	5.41	23.09	1.16	18.53
CoBEV [76]	Ground plane, Geometry	31.25	43.74	16.11	30.73	6.59	24.01	2.26	19.71
MOSE [10]	Ground plane, Geometry	25.62	—	11.04	—	—	—	—	—
M3D-RPN [2]	—	21.74	36.40	21.49	35.49	6.05	23.84	2.78	20.82
Kinematic3D [3]	—	23.56	37.05	13.85	28.58	5.82	23.06	1.27	18.92
MonoDLE [58]	—	19.08	33.72	19.76	33.07	3.77	21.42	2.31	19.55
MonoFlex [103]	—	32.01	44.37	13.86	28.47	10.86	27.39	0.97	18.18
BEVFormer [46]	—	25.98	39.51	8.81	24.67	3.87	21.84	0.84	18.42
BEVDepth [44]	—	9.00	25.80	3.59	20.39	0.85	19.38	0.30	17.84
MonoCon [52]	—	38.07	49.44	18.66	32.89	10.71	27.55	1.61	19.25
GroundMix [60]	—	47.72	57.26	32.12	43.64	12.86	29.37	3.90	21.06
YOLOv10-M3D N (Baseline)	—	27.67	41.05	14.12	30.21	8.57	24.72	0.92	18.60
LeAD-M3D N (Ours)	—	38.00	49.39	17.88	33.29	9.67	25.46	1.80	19.17
YOLOv10-M3D S (Baseline)	—	34.78	46.87	21.62	36.34	9.01	25.19	2.12	19.67
LeAD-M3D S (Ours)	—	43.52	53.89	26.78	40.50	13.33	28.59	4.16	21.25
YOLOv10-M3D M (Baseline)	—	43.23	53.68	30.65	43.62	11.88	27.53	3.88	21.12
LeAD-M3D M (Ours)	—	45.92	55.84	34.69	46.85	14.31	29.62	4.95	22.14
YOLOv10-M3D B (Baseline)	—	42.67	53.25	32.45	45.07	12.55	28.15	4.65	21.83
LeAD-M3D B (Ours)	—	46.30	56.14	34.75	46.90	15.05	30.13	5.40	22.41
YOLOv10-M3D X (Baseline)	—	44.06	54.38	31.31	44.18	13.87	29.33	4.12	21.54
LeAD-M3D X (Ours)	—	49.50	58.72	37.74	49.31	16.45	31.34	8.71	25.15

(2) It encourages the network to assign the highest class confidence to the prediction with the best overall 2D and 3D quality. This is crucial because, given multiple available predictions, the model must select only a single, optimal one for the final output; by incorporating 3D information, CM_{3D} ensures the selected prediction is globally the best, whereas the vanilla approach selects based purely on 2D overlap, neglecting critical 3D accuracy.

B.5. Qualitative results on Rope3D

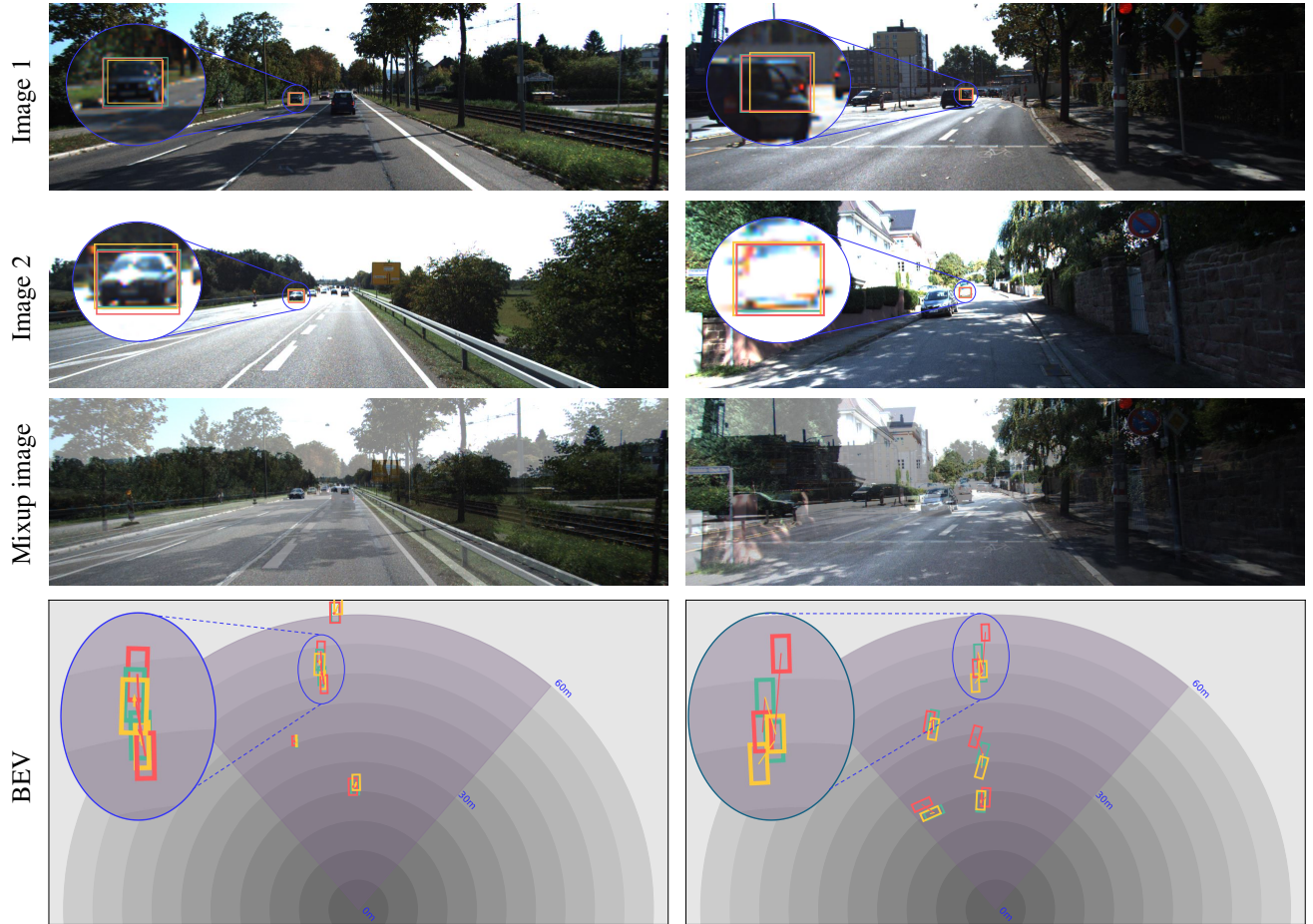
In Supplementary Fig. 7 we provide qualitative results on Rope3D [99]. Compared with KITTI [23], Rope3D spans a substantially wider depth range, which makes accurate monocular depth estimation even more challenging. Both methods exhibit some false negatives under heavy occlusion, but our LeAD-M3D consistently produces more accurate depth estimates than the YOLOv10-M3D; in many examples the improvement is large, with depth errors reduced by roughly 5–8 m relative to the baseline.

Supplementary Table 20. **3D detection accuracy on the Waymo [79] validation set using the same training and validation set as DEVIANT[39]**. Results are reported for Level 1 and Level 2 difficulty settings at IoU thresholds of 0.5 and 0.7.

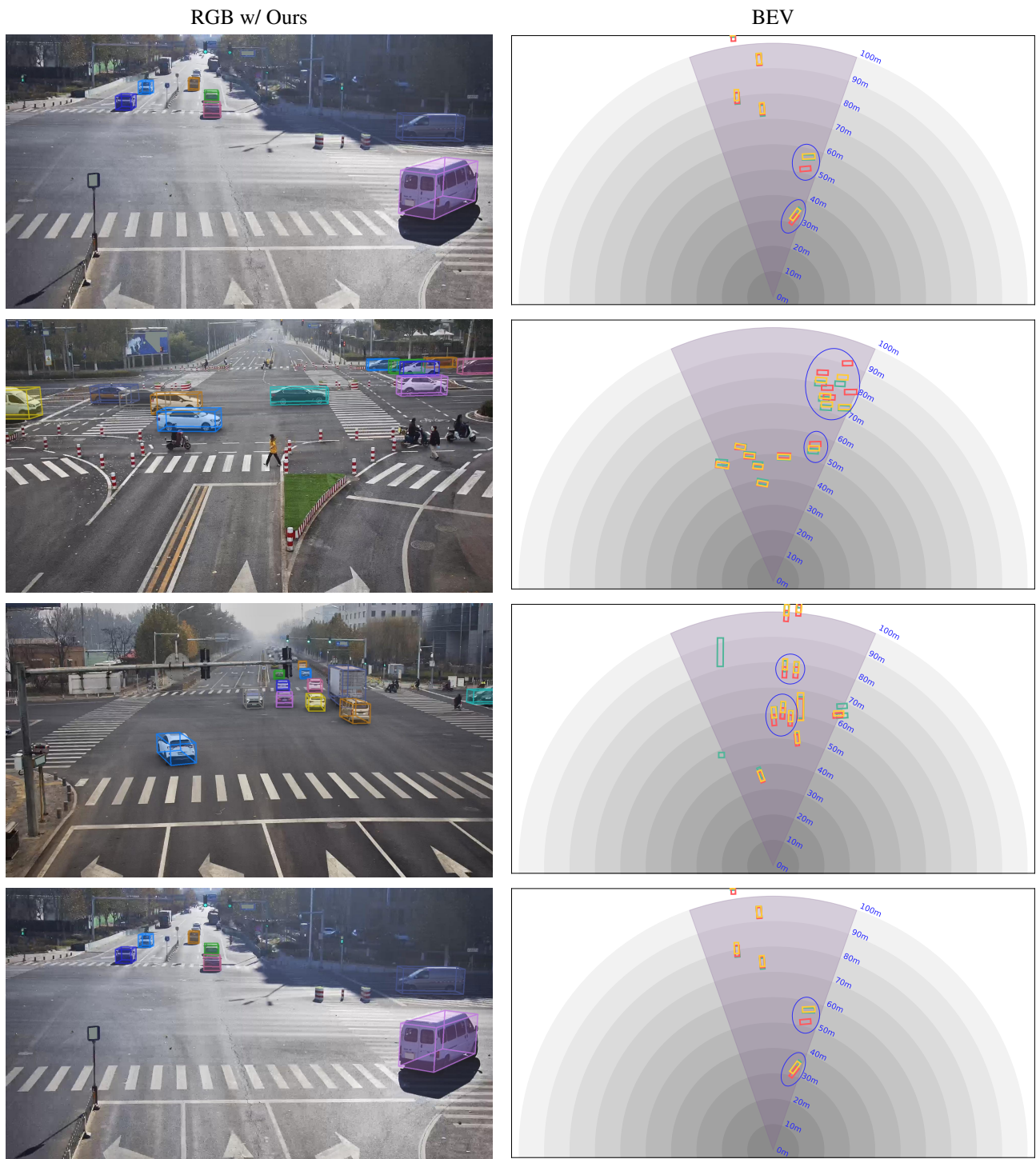
IoU	Method	Level 1								Level 2							
		AP _{3D} ↑				APH _{3D} ↑				AP _{3D} ↑				APH _{3D} ↑			
		All	0-30	30-50	50-∞	All	0-30	30-50	50-∞	All	0-30	30-50	50-∞	All	0-30	30-50	50-∞
0.7	YOLOv10-M3D N	2.34	6.00	0.73	0.07	2.31	5.93	0.72	0.07	2.06	5.90	0.66	0.05	2.04	5.83	0.66	0.05
	LeAD-M3D N	2.96	7.68	0.74	0.06	2.93	7.60	0.73	0.06	2.61	7.55	0.67	0.05	2.58	7.48	0.66	0.05
	YOLOv10-M3D S	2.71	7.00	0.97	0.09	2.68	6.92	0.96	0.09	2.39	6.88	0.88	0.07	2.37	6.81	0.87	0.07
	LeAD-M3D S	3.53	8.82	1.23	0.11	3.49	8.73	1.22	0.10	3.11	8.67	1.11	0.08	3.08	8.59	1.11	0.08
	YOLOv10-M3D M	2.95	8.73	1.05	0.09	2.93	8.65	1.04	0.09	2.61	8.60	0.95	0.07	2.58	8.52	0.95	0.07
	LeAD-M3D M	3.98	9.95	1.50	0.09	3.94	9.86	1.49	0.09	3.51	9.80	1.36	0.07	3.48	9.71	1.35	0.07
	YOLOv10-M3D B	3.13	8.19	1.29	0.10	3.10	8.11	1.28	0.09	2.76	8.06	1.17	0.07	2.73	7.99	1.16	0.07
	LeAD-M3D B	4.29	10.82	1.58	0.08	4.25	10.72	1.57	0.08	3.78	10.65	1.43	0.06	3.75	10.55	1.43	0.06
	YOLOv10-M3D X	3.34	8.93	1.39	0.12	3.30	8.84	1.38	0.12	2.95	8.80	1.26	0.09	2.92	8.71	1.26	0.09
	LeAD-M3D X	4.81	12.08	1.72	0.09	4.76	11.97	1.71	0.09	4.24	11.90	1.56	0.07	4.20	11.79	1.55	0.07
0.5	YOLOv10-M3D N	10.49	24.88	4.40	0.52	10.35	24.55	4.36	0.51	9.26	24.53	4.14	0.41	9.14	24.20	4.11	0.40
	LeAD-M3D N	12.14	28.72	4.58	0.49	12.00	28.38	4.54	0.48	10.73	28.32	4.15	0.38	10.60	27.99	4.11	0.37
	YOLOv10-M3D S	11.18	26.12	5.58	0.69	11.04	25.80	5.54	0.68	9.88	25.77	5.08	0.54	9.76	25.45	5.04	0.53
	LeAD-M3D S	13.24	30.59	6.41	0.81	13.09	30.23	6.36	0.80	12.08	30.17	5.81	0.64	11.94	29.82	5.76	0.63
	YOLOv10-M3D M	11.69	29.66	6.33	0.60	11.56	29.27	6.28	0.59	10.34	29.29	5.76	0.47	10.22	28.90	5.71	0.46
	LeAD-M3D M	14.55	33.54	7.11	0.63	14.40	33.20	7.07	0.62	12.86	33.12	6.68	0.50	12.74	32.78	6.64	0.49
	YOLOv10-M3D B	12.89	30.51	7.07	0.66	12.76	30.18	7.01	0.66	11.40	30.13	6.43	0.52	11.28	29.80	6.37	0.51
	LeAD-M3D B	15.04	34.87	7.47	0.47	14.88	34.51	7.42	0.47	13.29	34.44	6.76	0.37	13.15	34.07	6.71	0.37
	YOLOv10-M3D X	13.30	31.58	7.57	0.83	13.15	31.18	7.52	0.83	11.77	31.18	6.90	0.65	11.63	30.79	6.85	0.65
	LeAD-M3D X	16.46	38.42	8.30	0.58	16.28	38.01	8.25	0.58	14.54	37.93	7.55	0.46	14.39	37.52	7.50	0.45

Supplementary Table 21. **Comparison with SOTA monocular methods on the Waymo [79] validation set for the vehicle category (Level 1)**. Unlike the results in the main paper and Tab. 20, the same filtering is applied to both the training and validation sets here, as done in CaDDN [70]- **Time**: For a fair comparison, inference time is shown for batch size 1 in ms without TensorRT export (hardware: NVIDIA RTX 8000).

Method	Extra	Time ↓	AP _{3D} ^{0.5} ↑	APH _{3D} ^{0.5} ↑
CaDDN [70]	LiDAR	547.0	17.54	17.31
CMKD [28]	LiDAR	544.2	12.99	12.90
DID-M3D [65]	LiDAR	96.7	20.66	20.47
MonoNeRD [91]	LiDAR	1275.5	31.18	30.70
OccupancyM3D [66]	LiDAR	555.8	28.99	28.66
M3D-RPN [2]	—	65.4	3.79	3.63
LeAD-M3D X (Ours)	—	28.0	33.03	32.71



Supplementary Figure 6. **Qualitative comparison of matching strategies in the one-to-one head for the KITTI [23] training set: Vanilla 2D [83] (Baseline) vs. CM_{3D} (Ours).** The vanilla 2D matching strategy of the YOLOv10-M3D relies only on the projected 2D overlap, which can lead to suboptimal assignments in crowded or mixup-augmented scenes (*e.g.*, matching a prediction to a more distant ground truth object). In contrast, our proposed CM_{3D} strategy also incorporates the MGIoU [40] 3D bounding box overlap, leading to a better and more consistent overall assignment in 3D space. Best viewed in color and with zoom. Arrows point from the predicted 3D bounding boxes to the assigned 3D ground-truth bounding boxes. **Color coding:** Ground truth, prediction matched by the vanilla 2D approach, prediction matched by CM_{3D}, and field of view.



Supplementary Figure 7. **Qualitative results on the Rope3D [99] heterologous validation set.** LeAD-M3D X achieves more accurate depth estimates than YOLOv10-M3D X. Best viewed in color and with zoom. **BEV color coding:** Ground truth, YOLOv10-M3D X, LeAD-M3D X, and field of view.